Degradation of proton and carbon Bragg peaks due to density inhomogeneities

Master thesis in
Physics

Submitted by
Riccardo Dal Bello
born in Spilimbergo (Italy)

The thesis has been carried out at the
German Cancer Research Center (DKFZ)

under the supervision of
Prof. Dr. Peter Bachert
and
Prof. Dr. Oliver Jäkel

Department of Physics and Astronomy
University of Heidelberg
October 2016

Abstract Current analytical treatment planning of radiotherapy with protons and heavier ions neglect degradation of the sharp distal dose falloff (Bragg peak, BP) caused by inhomogeneous tissue. There is no appropriate model of this effect - which in turn allowed reduction of related dose deposition uncertainties. This thesis develops a comprehensive analytical model of the degradation resulting from static lung parenchyma. To do so, it adopts Monte Carlo (MC) simulations, validated by a series of transmission experiments on lung-like phantoms. Fluctuations in the water equivalent thickness (WET) were found the major degradation factor, contributing more than 75% (40%) to the distal falloff widening for a carbon (proton) BP - while energy and particle type were found to have no considerable impact. Also, it was found that the plateau of a clinical spread-out BP remains unaffected but the distal falloff is degraded and that the impact on the biological effect is driven by changes to the physical dose. The model was parametrized with respect to lung specific parameter (alveolar dimension and tissue density) and breathing state parameters (thickness traversed, air filling). Formulation of a Gaussian filter provided a unified, compact and complete description that can readily be implemented in a treatment planning system.

Zusammenfassung Der inverse Dosisverlauf ist ein charakteristisches Merkmal der Protonen- und Ionentherapie. Dieser kann in heterogenem Gewebe, insbesondere in der Lunge, jedoch deutlich abgeschwächt werden, wodurch Dosisunsicherheiten entstehen. Eine belastbare analytische Beschreibung des Effekts steht derzeit nicht zur Verfügung. In dieser Arbeit wurde daher auf Grundlage von Transmissions-Experimenten an Phantomen und Monte-Carlo Strahlentransport-Rechnungen ein einheitliches, kompaktes und umfassendes analytisches Modell dieser Strahl-Degradation entwickelt. Dabei stellte sich heraus, dass die Schwankungen in der wasseräquivalenten Dicke des Gewebes mit 75% (40%) den größten Anteil an der Verbreiterung des Dosisabfalls haben. Teilchentyp und energie spielen dagegen nur eine geringe bis keine Rolle. Die Dosis im Plateaubereich klinisch relevanter ausgedehnter Dosisverteilungen ("spread-out Bragg peaks") ist nicht betroffen, lediglich die distale Kante. Änderungen in der biologischen Dosis beruhen zum allergrößten Teil auf Änderungen der physikalischen Dosis. Das Modell umfasst lungenspezifische (Alveoli-Größe, Gewebedichte) und Atemzustandsparameter (durchstrahlte Länge, Luftfüllung). Durch eine Formulierung als Gaußfilter kann das Modell direkt in entsprechende, analytische Planungssysteme integriert werden.

to my family

Contents

List of Figures

List of Tables

Chapter 1

Introduction

Radiation therapy makes use of ionizing radiation in order to control cancer cells. In conventional therapy mostly high energy ($\sim MeV$) photon beams are used, which exhibit an exponential decrease of the dose with depth. Multiple fields are exploited to treat deep located tumors, resulting in high-dose in the target surrounded by the so-called dose bath to the normal tissue. Superior depth-dose profiles are obtained adopting proton and light ion beams ($A \lesssim 20$): these charged particles present a plateau with rather flat dose deposition before the maximum, which is reached about the end of their range and then followed by a steep fall-off to almost zero dose. This desirable depth-dose is referred to as "Bragg peak". The range can be controlled by varying the initial beam energy and extended volumes are treated with multiple energy steps resulting in the spread-out Bragg peak (SOBP).

The precision in the dose deposition of a Bragg peak leads, on the one hand, to the possibility of a better sparing of healthy tissue and, on the other hand, to stricter requirements on the precision and the accuracy of the treatment planning. In many treatment plans the characteristic shape of the Bragg peak is not altered and most of the efforts focus on the reduction of range uncertainties. A special case is given when the ion-beam traverses inhomogeneous tissues (e.g. lung, spongy bone). A series of experiments have shown that in these tissues, the characteristic depth-dose shape suffers from degradation [1,2], i.e. there is a reduced peak-to-plateau dose and a wider distal fall-off. To date, the degradation effect is not fully characterized and generally neglected in treatment planning. In particular, this effect is pronounced in lung tissue. To take it into consideration in the clinical practice at the Heidelberg ion-beam therapy center (HIT), a safe approach is adopted: pathways longer than $2 \div 3$ cm in lung tissue are preferably avoided, if unavoidable a fixed 20% uncertainty to the dose deposition is given[1]. In an ideal case, a complete lung model should be implemented to take in account the correct contribution of the degradation as well as range uncertainties due to respiratory motion; the latter should be further investigated, being this work focused on stationary lung parenchyma.

To date, few knowledge is available on the specific contributions of the physical sources of degradation, which understanding is fundamental in order to asses the

[1]Personal communication Dr. Malte Ellerbrock, HIT, Heidelberg

final effect. Recent experiments showed that a Gaussian filter applied to the nominal depth-dose distribution may result capable to reproduce a degraded Bragg-peak [3]; however, no systematic studies on the dependencies on the lung and beam parameters are available. Such information would allow a feasible implementation of the effect in a planning system.

This thesis presents a systematic investigation of the degradation effect on ^{1}p and ^{12}C beams through stationary lung parenchyma. The description aims to obtain an accurate and clinically applicable parametrization of the degradation to be implemented in specific lung cases.

To do so, a deeper understanding of the physics principles of ion beam therapy, in particular regarding the phenomena leading to the Bragg peak degradation, is fundamental. Such knowledge allows to correctly identify the origin of this effect towards a practical description and its prediction. Together with this, the lung tissue properties relevant for a degradation study should be investigated. These topics are treated in the first part of the thesis (Chapter 2).

To perform the systematic study, Monte Carlo (MC) radiation transport simulations are adopted as the most important tool, since they have been proved to successfully reproduce the transport of charged particles through complex targets in previous works [4]. Nevertheless, the complexity of the problem requires an experimental validation. For this, lung-like phantoms are analyzed and used in transmission experiments at HIT. The selected MC code is FLUKA, which is described in Chapter 3 together with the HIT facility and the phantoms. Moreover, this second part of the thesis reports in Chapter 4 the developments performed to accomplish the experiments .

The first experiment assesses the contributions of the different physical sources of the degradation. Knowing the specific weights, a practical and accurate model to reproduce stationary lung parenchyma in FLUKA is adopted. In the second experiment this model is tested through an experimental benchmark and then used in the third experiment to evaluate the dependencies of the degradation on beam and lung parameters. With the last experiment, specific clinically relevant consequences of degradation are investigated, including the effects on a SOBP and on the relative biological effectiveness (RBE). The third part of the thesis presents the experiments first (Chapter 5) and the respective results and discussion then (Chapter 6).

Finally, the last part is dedicated to the conclusions, the closing remarks and an outlook towards the applicability of the study.

Chapter 2

Background

In the following chapter the relevant background notions are reported. The first section focuses on the physics principles involved in ion beam therapy. The second section takes in account the specific problem of Bragg peak degradation due to lung tissue.

2.1 Physics of ion beam therapy

Radiation therapy is based on the response of biological tissue to the energy deposition of the radiation while traversing matter. Rather than the particles energy loss, the quantity that is of more interest in radiotherapy is the absorbed dose also referred as physical dose:

$$D = \frac{d\bar{E}_{ab}}{dm} \tag{2.1}$$

where $d\bar{E}_{ab}$ is the mean energy imparted by the ionizing radiation to the mass dm [5]. The used unit is the Gray, defined as $1Gy = 1J/1kg$. The behavior of (2.1) in traversing matter in the beam direction is usually referred as depth-dose profile and strongly depends on the type of interactions that the ionizing radiation undergoes. In Figure 2.1 the characteristic depth-dose profiles in water, medium commonly used as reference, for $\gamma, e^-, {}^1p, {}^{12}C$ beams at clinical E_{beam} are illustrated. Photon beams are the most widely used in clinical practice; for this type of radiation, after the so-called build-up region, there is an exponential decrease of the dose due to to statistical absorption of beam quanta. Electron beams lead to a rather wide region of high dose deposition and a wide tail, due to the light mass m_e, until the so-called practical range, after which no dose is deposited. On the other hand, ion-beams present a flat entrance in the dose deposition before reaching the so-called Bragg peak, where the dose maximum is found, followed by a sharp fall-off to the tail. The position of the Bragg peak can be precisely changed by varying the initial energy of the beam. The sharp depth-dose profile for ion-beams makes them particularly suitable for treatments of deep located tumors close to sensitive healthy tissues, especially when compared to photon beams [6]. Moreover, ${}^{12}C$ beams present a major advantage to ${}^1p$ beams. Despite the presence of a distal dose-tail due to fragmentation, ${}^{12}C$

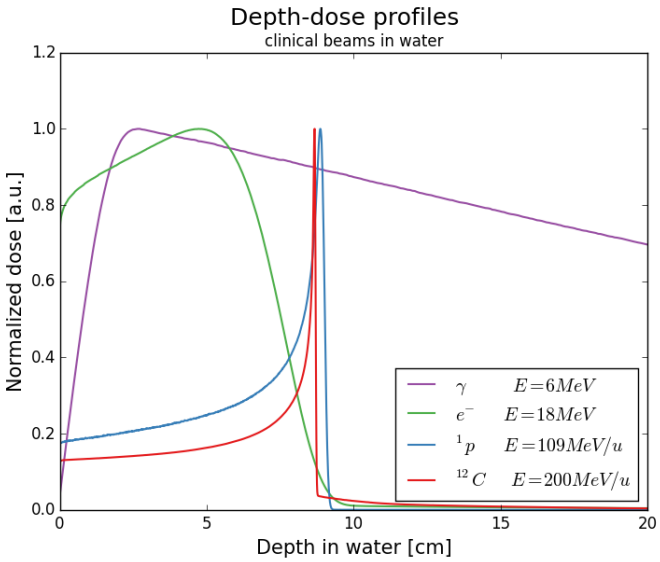

Figure 2.1: Characteristic dose deposition curves in water for ionizing radiation beams. E_{beam} in the clinical range. Incoming beams without energy spread, i.e. monochromatic beams. Normalized to the maximum. Simulations performed with FLUKA.

beams not only have a sharper peak due to the reduced straggling[1], but also have an enhanced biological effect due to the high density of the energy deposition in the peak region, which makes them particularly suitable for the treatment of radioresistent tumors [7]. The described depth-dose profile of ion-beams is the result of nuclear and electronic interactions between the projectile nuclei and the target nuclei and atoms. A detailed description is provided in the next paragraph 2.1.1.

2.1.1 Energy loss of ion beams in matter

Ion beams traveling through matter lose energy undergoing nuclear and electronic collisions, the latter giving the most relevant contribution as showed in Figure 2.2. To constrain the problem to a clinical application, one should consider the interactions for protons with $E_{kin}\,(^1p) \lesssim 250MeV$ and for carbons with $E_{kin}\,(^{12}C) \lesssim 450MeV/u$. Given $E_{tot} = E_{kin} + m_0c^2$, these maximum energies translate into the velocities:

$$\beta = \frac{pc}{E_{tot}} = \frac{\sqrt{E_{tot}^2 - m_0^2c^4}}{E_{tot}} \simeq \begin{cases} 0.6, & ^1p \\ 0.7, & ^{12}C \end{cases} \tag{2.2}$$

therefore a relativistic approach is necessary at most in the entrance channel, a smooth transition between the relativistic and lower energy models is required in a consistent Monte Carlo radiation transport code.

The specific energy loss in a single collision and the time between single collisions are stochastic processes. The typical distance between consecutive collisions of

[1]The straggling depends on the mass of the projectile, one has approximately: $\frac{m_{^1p}}{m_{^{12}C}} \simeq \frac{1}{12}$

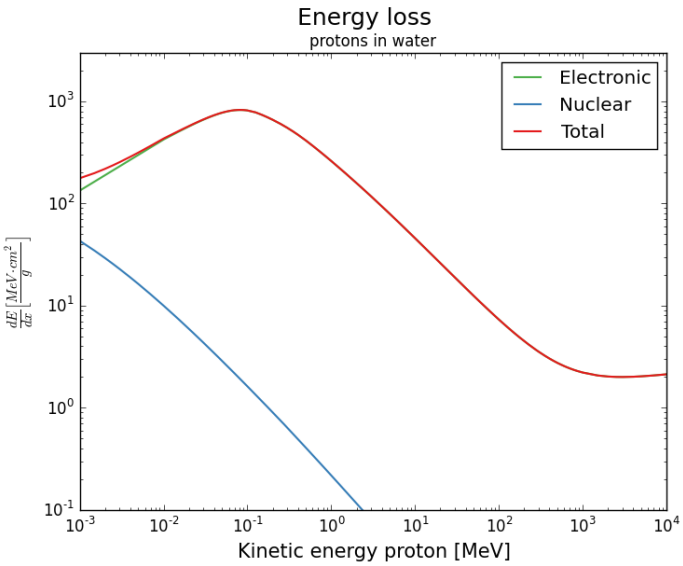

Figure 2.2: Stopping power for protons in water as function of the kinetic energy. Source data from the NIST database [8]. The electronic energy loss is the predominant effect, nuclear energy loss increases at lower energies at the end of the range.

relativistic ions is in the order of $\lambda \lesssim 10^{-9}m$ in water[2]. On a macroscopic scale d, of interest in ion-beam therapy, it holds $d \gg \lambda$; one is therefore interested in the mean energy loss per unit path length and at higher momenta of the distribution. In the moderate relativistic regime limited by (2.2), the mean energy loss of charged particles by electronic collisions is well described by the Bethe-Bloch equation [10]:

$$-\left\langle \frac{dE}{dz} \right\rangle = 4\pi N_A r_e^2 m_e c^2 \rho \cdot \frac{Z}{A} \cdot \frac{z_p^2}{\beta^2} \cdot \left[\frac{1}{2} \ln \left(\frac{2m_e c^2 \beta^2 T_{max}}{I^2 \cdot (1-\beta^2)} \right) - \beta^2 - \frac{\delta}{2} - \frac{C}{Z} \right] \quad (2.3)$$

where N_A is the Avogadro number, e, m_e and r_e are respectively the charge, mass and the classic radius[3] of the electron, ρ is the density of the target material, Z, A refer to the target material, z_p and β to the projectile and T_{max} is the maximum kinetic energy which can be imparted to a free electron in a single collision[4]. In order to have a compact form of (2.3) one introduces the mean ionization potential I of the target. This quantum-mechanical quantity is defined from the strength of the dipole oscillation of the target atoms: $\ln(I) = \sum_n f_n \cdot \ln(E_n)$, $f_n = \frac{2mE_n}{\hbar^2 Z_t} \left| \sum_i < n|x_j|0 > \right|^2$ [11]. The analytic calculation of I is possible only for hydrogen-like atoms, numerical approaches are suitable for pure elements but fail to achieve a sufficient precision for molecules, introducing one of the major range uncertainties in particle therapy. Novel approaches aim to reduce the uncertainties in the in-vivo estimation of I, e.g. by using dual-energy computed tomography [12]. Finally, δ and C are respectively

[2]The single interaction time is $\tau \leq \langle \nu \rangle^{-1}$, where in first approximation $\langle \nu \rangle = I \cdot \hbar^{-1}$ [9], for water $I \simeq 75eV$, considering the limit $\beta = 1$ one has $\lambda \leq \beta\tau \simeq \beta \cdot \hbar \cdot I^{-1}$

[3]$r_e = \frac{1}{4\pi\epsilon_0} \frac{e^2}{m_e c^2}$

[4]$T_{max} = \frac{2m_e c^2 \beta^2 \gamma^2}{1+2\gamma m_e/M+(m_e/M)^2}$

a density correction in the relativistic regime and a shell correction relevant when β approaches the velocity of the shell electrons. Also, the (2.3) can be derived starting from the classical calculation of Bohr and introducing the Bethe quantum corrections [5]. Higher order corrections lead to the final expression [11].

Due to the statistical nature of the process, each beam particle stops at a specific depth in the target leading to a range distribution. The 80% of the maximum dose in the fall-off of the Bragg peak can be proven to be a good estimator of the mean range of the beam particles [13], the consistency of this estimator in lung tissue is analyzed in the section 6.1.1. Again, the (2.3) describes the mean energy loss of charged particles and can be used to calculate the range of a charged particle with the so-called CSDA (continuous slowing down approach) approximation [5]:

$$R_{CSDA} = \int_{E_0}^{0} \left\langle \frac{dE}{dz} \right\rangle^{-1} dE \tag{2.4}$$

Finally, for an ion with initial energy E_0, about the depth given by (2.4), the Bragg peak maximum is reached. The shape reported in Figure 2.1 is described punctually by (2.3). The different widening of the dose deposition for ^1p and ^{12}C is the matter of discussion of the next paragraph.

2.1.2 Range straggling

It has been pointed out that the energy loss for ions in matter is a statistical process. The distribution had so far being characterized with the mean (2.3), here it is of interest the second moment of the distribution, i.e. the variance. If it is assumed that for a set of projectiles the mean energy loss $d\bar{E}$ in dz, for the whole set holds [9]:

$$\frac{d}{dz}\langle \left(E - \bar{E}\right)^2 \rangle = 4\pi z_p^2 e^4 NZ \tag{2.5}$$

where higher order corrections are neglected. The (2.5) can be integrated on a finite thickness Δz giving the variance of the energy distribution after traversing the given thickness:

$$\mathrm{Var}[E] = 4\pi z_p^2 e^4 NZ\Delta z. \tag{2.6}$$

Considering only the electronic energy loss, i.e. the dominant contribution in Figure 2.2, the energy of the projectiles has a Gaussian distribution with variance given by (2.6). The nuclear collisions give a small contribution in the mean energy loss but an appreciable influence in the fluctuations, resulting in a tail of the Gaussian distribution at high energy loss values [9]. The energy straggling is directly related to the range straggling, in particular for an energy loss dE in dz it holds:

$$\langle \left(E - \bar{E}\right)^2 \rangle = \left(\frac{dE}{dz}\right)^2 \cdot \langle (r_{res} - \bar{r}_{res})^2 \rangle \tag{2.7}$$

where $r_{res}, \bar{r}_{res}$ are the residual ranges of the particles and their mean. Integrating the (2.7) one obtains the general relation for the variance of the range distribution

for particles with initial energy E_0 [9]:

$$\langle \left(R - \bar{R}\right)^2 \rangle = 4\pi z_p^2 e^4 N Z \int_{E_0}^{0} \left(\frac{dE}{dz}\right)^{-3} dE. \tag{2.8}$$

Now, assuming the approximation of a Gaussian distribution of the range distribution, one can obtain a simple relation between the variance of the range distribution σ_R^2, the mean R and the mass of the projectile M [14]:

$$\frac{\sigma_R}{R} \propto \frac{1}{\sqrt{M}}. \tag{2.9}$$

Now, comparing ^1p and ^{12}C Bragg peaks with the same range in the light of the (2.9), one expects for Carbon ions a widening of the peak about $\sqrt{12} \simeq 3.5$ times smaller. This phenomenon is observed qualitatively in Figure 2.1 and the specific contribution in lung tissue will be analyzed in the section 5.1.

2.1.3 Scattering effects

Together with the inelastic collision with electrons leading to the (2.3)-(2.9), ion-beams traveling through matter undergo elastic Coulomb collisions with the target nuclei themselves. The latter result in a negligible energy loss; nevertheless, these are highly relevant phenomena in radiotherapy since they lead to the creation of a transverse displacement and an angular distribution in the beam particles. The elastic Coulomb interactions with the target nuclei are highly frequent events and are modeled under the name multiple Coulomb scattering (MCS). Depending on the assumed approximation, the MCS can be modeled with the Molière theory [15] or the Lewis theory [16]. When considering the angular distribution in the beam direction, the two theories differ slightly in the tails at big angular deflections, the common central dominant term is Gaussian distributed with $\langle \theta \rangle = 0$ and, according to Molière, a variance:

$$\langle \theta^2 \rangle = \left\{ \frac{19.2}{\beta pc} \cdot z_p \cdot \sqrt{\frac{z}{X_0}} \cdot \left[1 + 0.038 \cdot \ln\left(\frac{z}{X_0}\right) \right] \right\}^2 \tag{2.10}$$

with pc in $[MeV]$ and θ in $[rad]$, being z the travelled path in the original direction and X_0 the radiation length. The Molière theory has the advantage that it is build on few material-dependent parameters, χ_{cc} and b_c, and that could be expanded in order to get the distributions of any physical quantity of interest. In particular, it is of interest the lateral displacement to the original direction. Given a specific value from the angular distribution, one can compute the lateral displacement r according to [17]:

$$r = z \cdot \sin\left(\frac{\theta}{2}\right) \cdot \left(1 - \frac{f_1\left(\theta, b_c\right)}{2} \cdot \chi_{cc} \cdot z + \frac{f_2\left(\theta, b_c\right)}{6} \cdot \chi_{cc}^2 \cdot z^2 \right) \tag{2.11}$$

where f_1, f_2 are complex relations derived considering the sole Gaussian term with the variance (2.10). Single and plural nuclear scattering (NS) events leading to rare

big angular deflections are not included in the MCS theories. NS results in heavier tails of the real $p(\theta)$ distribution; however, it does not affec the central Gaussian description [9].

Now, comparing in first approximation the numerical values of (2.10) for ^1p and ^{12}C beams in the limits given by (2.2)[5] through the same material, one has:

$$\langle\theta^2\rangle \propto \frac{z_p^2}{(\beta pc)^2} = \frac{z_p^2}{(\beta^2 E_{tot})^2} \overset{\propto}{\sim} \frac{z_p^2}{A^2} = \begin{cases} 1, & {}^1p \\ 0.25, & {}^{12}C \end{cases} \tag{2.12}$$

therefore, one has about ~ 4 times reduced MCS for carbons compared to protons, leading to a better collimation of the beam inside the target and thus less lateral dose when performing a treatment. Finally, the result of (2.12) could be of interest when plugged into (2.11): in a lung tissue, as reported in the next section 2.2, a lateral displacement of a beam particle could result into a different value of (2.3) and therefore a different residual range.

2.2 Bragg peak degradation due to lung tissue

The depth-dose distributions presented in Figure 2.1 could be severely altered when the beam travels through an heterogeneous target, such as which is found in the human lung. Recent studies showed the effects on the dose deposition for photon beams in lung tissue, suggesting that a better consistency is achieved adopting Monte Carlo simulations transporting the radiation through a fine-resolved lung-like structure compared to analytic calculations on the mean density model resulting from a clinical CT [4]. The differences are mainly the result of different beam attenuation through the sub-structures of the lung, which are neglected in the mean density model currently adopted in clinical practice. Given the precision of the dose deposition of a Bragg peak compared to the photon case, the deviations are expected to be more significant for ion-beams. The resulting effect is the so-called *degradation*, which could lead to a loss of the highly advantageous depth-dose shape [1]. In the following paragraphs, first the microscopic structure of the human lung leading to the degradation is analyzed, then the resulting effect on the Bragg curve.

2.2.1 Structure of the human lung

The human lung is composed mainly of two materials with a dramatic density difference: soft tissue ($\rho_S \approx \rho_{H_2O} = 1\,\mathrm{g/cm^3}$) and air ($\rho_A \approx 10^{-3}\,\mathrm{g/cm^3}$). The spatial distribution of these two materials is highly complex and the dimensions of the structures range from the order of few centimeters (bronchi, arteries and veins; resolvable with a clinical CT) down to hundred of micrometers (alveoli; resolvable only with a μCT) [4]. The specific positions of the single structures, and therefore the materials, are patient and time dependent resulting in an intrinsic and unpredictable randomness of the lung-tissue, which basic structures are shown in Figure 2.3a. On

[5]Here it is assumed $E_{tot} = \gamma m_0 c \approx m_0 c^2 \propto A$ for $\gamma \approx 1$, having at most $\gamma(\beta = 0.7) = 1.4$

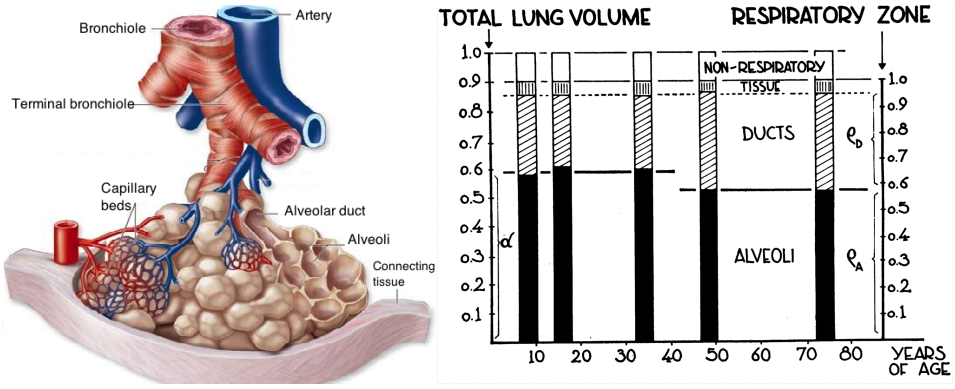

(a) (b)

Figure 2.3: (a) Representation of the terminal structure of the human lung with not-in-scale microscopic structures. Modified from [18]. Bronchial and arterial structures are surrounded by alveolar ducts and alveoli, which constitute the largest volume fraction of the lung, as shown in (b) [19]

Table 2.1: Lung parameters from the studies [4, 20, 21].

Study	V_{lung} (l_{cube})	f_A	ρ_{tot}	$d_{alveoli}$
L. Liang et al. (2007)	10^3cm^3 (10 cm)	0.74	$0.26\,\text{g/cm}^3$	$\gtrsim 100\,\mu m$
U. Titt et al. (2015)	$125\,\text{cm}^3$ (5 cm)	~ 0.7	$0.27\,\text{g/cm}^3$	$500\,\mu m$
M. Ochs et al. (2004)	$1.5 \cdot 10^3 \text{cm}^3$ (11.5 cm)	0.64	$0.36\,\text{g/cm}^3$	$200\,\mu m$
Gammex Lung (see section 3.3)	– (–)	0.73	$0.39\,\text{g/cm}^3$	$469\,\mu m$

a macroscopic scale, the lung is a spongy and heterogeneous organ, which volume is covered about 10% by CT-resolvable airways and blood vessels and about 90% by the respiratory zone [19]. The alveoli, air-filled structures responsible for the exchange $CO_2 \leftrightarrows O_2$, cover the most important fraction of the respiratory zone (Figure 2.3b). Special attention is therefore given to the characterization of the alveoli: the typical geometry resemble a honeycomb cell, however, for most of the purposes it could be characterized by the average diameter and modeled as a sphere [19] or as a cylinder [4]. Several studies aimed to an estimation of lung and alveolar parameters, a selection of these is reported in Table 2.1. The total volume of the lung V_{lung} ($l_{cube} = \sqrt[3]{V_{lung}}$), the air filling fraction f_A, the overall density ρ_{tot} and the diameter of the alveoli $d_{alveoli}$ depend on the selected study. Rather than to infer average values, Table 2.1 should give asses to the parameter's range of variability.

2.2.2 Resulting degradation

Early studies showed that the Bragg peaks suffer from degradation due to inhomogeneities and that available analytical models fail to predict the effect, which can be better reproduced by MC simulations [1]. The early experimental results showed that a degraded Bragg peak present reduced peak dose and wider distal fall-off. Such effects are the result of MCS, NS and the randomness of the inhomogeneities, leading to different attenuation for different beam particle, and therefore a wider (2.8). The specific contribution of the different effects in lung tissue is analyzed in Section 5.1. Previous studies where performed at PSI (Villigen, Switzerland) in order to implement in analytic dose calculations the effect of thick[6] density inhomogeneities [22,23]. However, no further systematic investigations on inhomogeneities in the sub-millimeter scale were performed. More recently the specific contribution to the degradation of MCS and NS for ^1p beams through regular check-board bone-air interfaces was investigated, showing that MCS is the dominant effect, i.e. NS has a $\sim 5\%$ contribution [2]. Finally, it was shown that a simple binomial model resulting in a convolution of the undegraded Bragg peak with a Gaussian filter is capable to reproduce ion-beam depth-dose distributions downstream lung tissue [3]. Given the undegraded depth-dose $D^{(0)}(z)$, the degraded one can be described by:

$$D^{\text{deg}}(z) = D^{(0)}(z) \otimes \mathcal{N}(z \mid \mu, \sigma^2) = \int_{t \in \Omega} dt \cdot D^{(0)}(t) \cdot \frac{1}{\sqrt{2\pi}\sigma} e^{-\frac{(z-t-\mu)^2}{2\sigma^2}} \tag{2.13}$$

where μ can be interpreted as the water equivalent thickness of the lung tissue and σ^2 as a degradation parameter. The description via a Gaussian filter has the practical advantage of a possible direct implementation in an analytic dose calculation algorithm. However, to date, no knowledge is available on the dependencies of (μ, σ^2) on the beam or the tissue parameters, e.g. the E_0 and the entries in the Table 2.1. The objective of this study is to verify the range of applicability of the (2.13) and to provide the relevant dependencies of (μ, σ^2), aiming to a practical implementation in analytic dose calculation tools, which are currently neglecting the degradation effect.

[6] Thick: structures in the order of centimeters resolvable with a clinical CT

Chapter 3

Materials and Methods

In the following chapter the description of the adopted techniques and the facility is reported. The study is performed through the use a specific radiation transport simulation code, which characteristics, advantages and limitations are analyzed. The experimental part of the project is performed at the Heidelberg ion therapy center. The facility is described hereinafter, together with the irradiated phantoms.

3.1 The FLUKA Monte Carlo code

Monte Carlo radiation transport simulations are adopted as the fundamental tool to perform the systematic study of Bragg peak degradation. Specifically, the FLUKA MC is chosen, which has been used since 2006 for multiple applications in the preparation of the clinical operation of the proton and carbon ion therapy facility HIT [24]. MC simulations have been proved to successfully reproduce the transport of charged particles through complex lung-like targets in previous works, leading to more accurate results compared to forward analytic calculations [4].

FLUKA is a multipurpose tool for calculations of particle transport and interactions with matter. It covers an extended range of applications from proton and electron accelerator shielding to target design, from calorimetry to dosimetry and detector studies, including, among others fields such as cosmic rays and neutrino physics, as well radiation therapy [25, 26]. The original development of this Monte Carlo code started in the '70s at the European Organization for Nuclear Research (CERN, Geneva, Switzerland) to perform accurate shielding studies of high energy proton machines. Due to its superior high-energy hadron generator, the interest on this code spread to different research areas leading to further specialized developing. The current available FLUKA version is usually referred as the *third generation*, which maintenance was entirely supported by the National Institute for Nuclear Physics (INFN, Rome, Italy). The work presented in the current thesis is conducted with the last respin FLUKA 2011.2c.4. The recent versions of FLUKA include a detailed physics of ^{1}p and ^{12}C interactions down to the energies used in ion-beam therapy together with implementations oriented to radiotherapy (e.g. DICOM import module). The details about the physics in this MC code are presented in the next section 3.1.1.

The simulation input is provided by the user through the so-called *cards*. Advanced options are treated with user routines, described in section 3.1.2

The simulation environment is implemented in FLUKA using a combinatorial geometry. This allows for accuracy and efficiency in the transport of particles through different regions. Multiple basic geometrical objects are pre-implemented in the code, which can be combined into regions where a specific material has to be unequivocally assigned. The particles are transported with sampling of the respective interactions within each region and the consistency of the physics (e.g. energy and momentum conservation) is verified at each boundary crossing. It is suggested by the developers the simulation of infinite intercepting geometrical bodies rather than closed bodies, to fully exploit the efficiency of the combinatorial geometry and allow for the maximum accuracy in the transport. User defined materials can be implemented through the use of the COMPOUND card, where the atomic content can be given in absolute, volume or mass ratios. Moreover, the card MAT-PROP allows for additional properties of the user-defined materials including density and I-value. The latter, if not given, is automatically calculated according to Seltzer-Berger [27].

3.1.1 Physics implementation

Being a multipurpose code, the implemented physics in FLUKA ranges beyond the requirements of applications in radiotherapy: e.g. the transport of charged particles is possible up to energies in the order of PeV. The code includes an implementation of sound and modern physical models allowing for final predictions obtained with a minimal set of free parameter. There is no direct access to the tuning of the physical models, which are maintained and updated with the releases. The user should rather define the range of applicability to optimize the simulation to the specific setup. This is done with the input of the DEFAULTS card. In the current work the *precision* defaults are adopted, which relevant features are:

- transport of electrons, positrons and photons activated together with Rayleigh scattering and inelastic form factor corrections to Compton scattering;
- low-energy neutron transport activated together with fully analogue absorption for low-energy neutrons;
- particle transport threshold set at $100keV$ (except neutrons);
- multiple scattering threshold at minimum allowed energy both for primary and secondary charged particles;
- δ-ray production activated with threshold $100keV$;
- energy loss fluctuation activated for both hadrons/muons and EM particles;
- fraction of the kinetic energy to be lost in a step set at 0.05;
- heavy fragments transport activated.

The particles with kinetic energy below the transport threshold are ranged to rest in one step with uniform energy deposition. This parameter together with the fraction of energy lost in a single step have a strong dependency on the simulation time. A proper choice of these values results in a compromise between computation time and accuracy of the result. The multiple scattering is implemented with an extension of the Moliere theory resulting, among other parameters, in an explicit calculation of the lateral displacement (2.11) at each step. To allow for a complete simulation of heavy ion transport and fragmentation, the executable files are linked to the libraries DPMJET-III and RQMD.

Certain physic processes can be deactivated to study specific situations. This is the case, for example, of the fluctuations in the energy loss (2.3) leading to the range straggling (2.9). The card IONFLUCT can be used to set to zero the value of (2.6) and therefore simulate the sole CSDA. This leads to an un-physical simulation, which, however, is suitable to assess the different origins and contributions to the widening of a Bragg peak. Full physics it is used in the simulations through out this work, when the energy loss fluctuations are turned off it is explicitly mentioned.

3.1.2 User routines

The coding of user routines allows for additional flexibility of the MC simulations. The FLUKA code is based on a FORTRAN77 implementation, which can be extended for problem-specific input or output through the coding of such routines. For the scope of this work two routines result of particular interest: source.f and mgdraw.f.

The first allows to simulate a beam source with a complete flexibility, without the limitations given by the SOURCE card. This is necessary, for example, in order to simulate the plan of a SOBP. In this case, a source with multiple beam energies and specific weights should be simulated, which is not available through the standard input card. To do so, a user routine should sample the particle energies from a proper distribution and then inject the primaries into the stack. Moreover, the source routine can be used to simulate a mixed field sampling the particle properties from a phase space.

The mgdraw routine allows to follow the tracking and the interactions of every particle and therefore defining with high freedom a user detector. This is particularly suitable to infer the relative biological effectiveness (RBE) associated to the deposited physical dose. The mgdraw routine allows to execute user code connected to specific transport events, e.g. a boundary crossing. Therefore, the complete phase space together with the LET spectrum can be scored at specific points of the geometry to produce a user-defined output. The data can then be converted through dedicated models into RBE and therefore biological dose.

3.2 The HIT facility

The experimental part of the project is performed at the Heidelberg ion therapy center (Heidelberg, Germany). A schematic overview of the center with a description

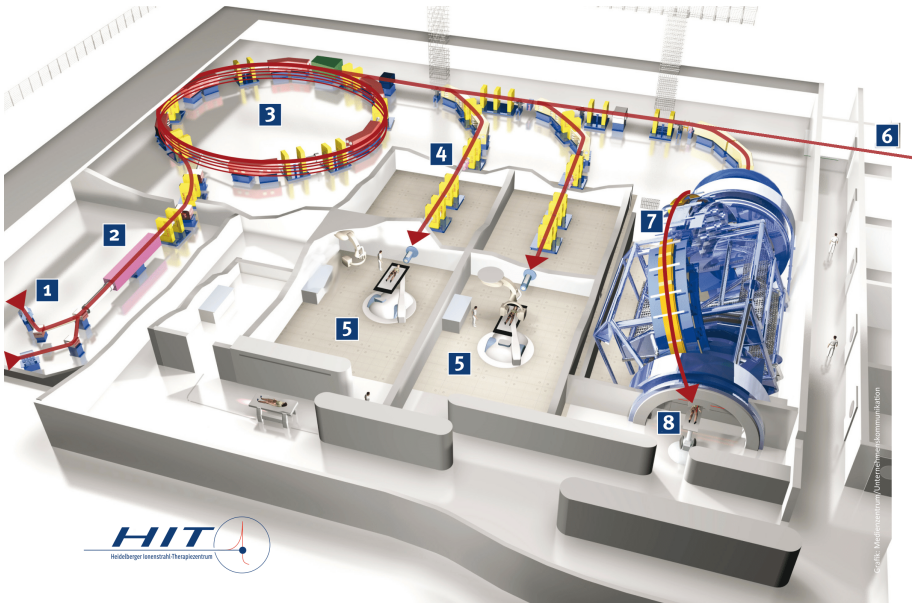

Figure 3.1: The HIT facility. The schematic view follows the production, acceleration and delivery of the ion beam: the sources (1) inject the ions in the linear accelerators (2), which provide the beam the initial enegy to be injected in the synchrotron (3). Here the beam is accelerated to the desired energy and then delivered through magnets (4) to the treatment rooms (5) or to the experimental room (6). The gantry (7) provides additional flexibility in the dedicated treatment room (8). Modified from [28].

of the relevant components of the facility is reported in Figure 3.1. HIT has been the first dedicated and hospital-based irradiation facility for protons and heavier ions in Europe [29]. The operation started in November 2009 and it has been planned to treat $>$ 1000 patients per year. This synchrotron-driven facility is based on the technical developments investigated at Gesellschaft fuer Schwerionenforschung (GSI, Darmstadt, Germany) together with Simens AG (Berlin, Germany). HIT takes the full advantage of the highly desirable depth-dose distribution of ion beams with the active beam delivery method coupled with an intensity-controlled rasterscan technique. This treatment modality allows to precisely deliver the dose in steps to the desired volume. The target is divided into multiple depth slices according to a WET map. Each slice is then sub-divided into voxels, the so-called raster points. The treatment plan is then optimized on the matrix of the raster points. To perform such treatments, a superior control and flexibility of the physical properties of the beam are required. The active beam scanning is provided by the synchrotron, which allows to accelerate the beam to the required energy in precise steps (255 steps available, energies up to $221 MeV$ for ^1p and $430 MeV/u$ for ^{12}C). The active beam delivery is technically superior to the passive alternative [1] providing a clean delivery system, i.e. the activation and the presence of secondaries in the beam are dramatically reduced.

[1] In a passive delivery the high energy beam is modulated through a compensator

Within a slice, the intensity-modulated raster-point scanning is achieved through dedicated vertical and horizontal scanning magnets coupled with the 15 available intensity steps. Finally, the focus size can be controlled in 6 steps providing a Gaussian FWHM ranging from $3mm$ to $35mm$ at the isocenter, depending on the beam type and energy.

3.2.1 Beam application monitoring system

The delivered beam is controlled with the beam application monitoring system (BAMS) positioned at the beam nozzle and shown in Figure 3.2. The system is available both

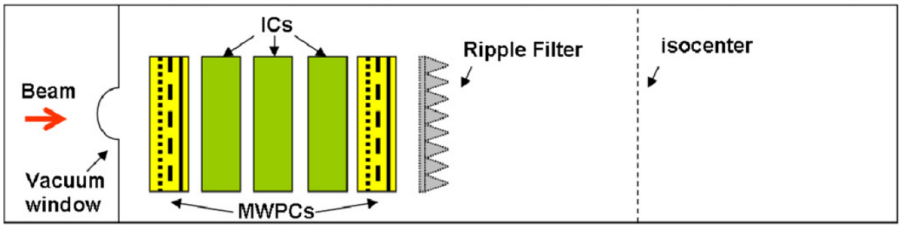

Figure 3.2: Representation of the HIT beam nozzle with the permanent elements: vacuum window, multi-wire proportional chambers (MWPCs) and ionization chambers (ICs). Additionally, the ripple filter could be inserted [24].

in the treatment and experimental rooms. The presence of the BAMS implies interactions between the detectors and the particles, which up to this point travel in vacuum. These interactions modify the phase space of the beam: e.g. the energy distribution might not be properly described by a Gaussian of sole primary particles; this is in particular valid for ^{12}C ions. Moreover, the presence of the BAMS introduces an offset in the range respect to an hypothetical mono-energetic beam at the nominal energy.

3.2.2 Peakfinder experiments

The experimental data is acquired with the Peakfinder water column (PTW, Freiburg, Germany). A schematic view of the internal structure of the detector is reported in Figure 3.3, whereas the external view in the experimental setup is given in Figure 5.2. The detector allows to measure the dose deposition in water for proton and carbon beams with high precision ($\delta_z = 100\mu m$ absolute position and $\delta_z = 10\mu m$ relative position). The measurement is based on the presence of two ionization cambers (ICs) enclosing a water column of variable depth. The water column and the position of the second ionization chamber are controlled with a mechanic belt. The depth-dose distributions are acquired by varying the length of the water column and reading out the ICs while the accelerator delivers the beam. Dedicated PTW software it is used to activate the mechanic belt and synchronize the readout. The operation of the Peakfinder requires about $\sim 5s$ for the acquisition of each data point; the time necessary to scan a Bragg peak is therefore determined by the range inspected

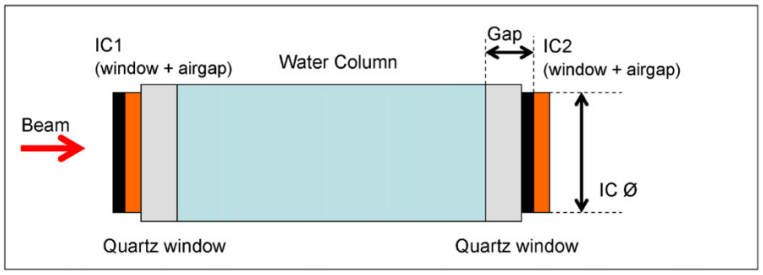

Figure 3.3: Representation of the internal structure of the Peakfinder water column. The relevant components are shown: the signal is detected by the ionization chambers (IC1 and IC2), which lay about the water column encompassed by two quartz windows [24].

in water and the resolution used. The output returns the relative readout of IC2 respect to IC1, assuming that during the measurement the dose at the entrance channel is constant. The data is therefore especially useful to measure differences in water equivalent thicknesses of phantoms placed upstream the detector, providing a direct measurement with the shift in the Bragg-peak position. On the other hand, to compare the data with MC simulations a conversion factor should be applied since the Peakfinder does not provide an absolute dose measurement. Moreover, same Peakfinder measurements at different energy steps [2] could not be directly compared due to the fact that the data is normalized to the entrance point, which absolute dose differs according to the energy step. Again, a conversion factor should be applied.

3.3 Lung-like phantoms

The connection between the experiments and the simulations introduced in the previous sections is provided by the selection of the lung-like phantoms and their implementation in the MC numerical experiments.

Different approaches have been adopted in previous studies. The use of a real pig lung allows for a highly realistic Bragg peak degradation, but as well it implies technical difficulties in the experimental setup, reduced flexibility, unlikely reproducibility and high uncertainty on the phantom internal structure to be implemented in MC [3]. The analysis of a real lung degradation is the final aim of the project, but the use of such setup is not applicable for a systematic study. The use of customized 3D-printed phantoms allows for a exact knowledge of the designed internal structure with a direct MC implementation, but it comes with limits in the complexity of the phantoms due to the printer precision [20]. In this thesis a compromise is selected between the knowledge of the internal structures, the reproducibility of the experiments and the affinity to the geometrical complexity of a real lung. To do so, a selection of lung-like porous materials is performed. Nonetheless, the applicability of 3D-printed phantoms is investigated.

[2] e.g. single peaks within a SOBP

3.3.1 Porous materials

Ready-to-use porous materials are adopted to reproduce stationary lung parenchyma leading to Bragg peak degradation. The aim is to perform transmission experiments using solid phantoms easy to shape, having a randomized porous internal structure with properties following Table 2.1 and that allow for reproducibility of the experiments. These requirements lead to the investigation of two classes of phantoms: Gammex tissue equivalent materials (Gammex Inc., now part of Sun Nuclear, Melbourne, USA) juxtaposed to rigid polymer foams and aerated concrete.

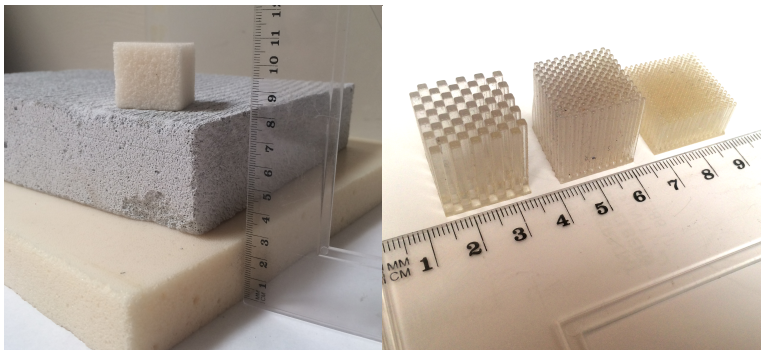

(a) (b)

Figure 3.4: (a) Porous materials. From the top to the bottom: Phantom B, Phantom C and Phantom A. (b) 3D printed check-board phantoms. Dimension internal structures from the left to the right: $2mm$, $1mm$ and $0.75mm$.

The Gammex materials are commercially available tissue surrogates commonly adopted in conventional radiotherapy for calibration and quality assurance purposes. These epoxy-based compounds are developed to closely reproduce radiological properties of specific tissues, including lung among others. The accuracy in scattering and absorption is guaranteed within 1% of living tissue for electron and photon applications between $0.01MeV$ and $100MeV$ [30]. No data is available concerning ^{1}p and ^{12}C beams, however, the geometrical structure and the total density are designed to reproduce lung parenchyma making the Gammex lung phantoms the first choice for the transmission experiments. Specifically, two different lung surrogate are available: 1x Gammex lung 455 plate (dimensions: 30x30x10(h)cm^3, serial no. 4556473 2) from now on referred as "Phantom A"; 1x Gammex lung small brick (dimensions: 3x3x3cm^3, serial no. unknown) from now on referred as "Phantom B". The two materials are shown respectively at the bottom and at the top of Figure 3.4a. The phantoms A and B are available in the $3cm$ thickness design, resulting in two parallel smooth surfaces. The internal structure is porous with air cavities enclosed in the solid part. The material composition is binary, i.e. solely composed by air cavities and solid part. The nominal density of Phantom A is $0.39g/cm^3$, no exact information is provided by the manufacturer regarding the cavities dimension, air filling ratio and elemental composition. An approximate estimate of the latter is given in a previous study [31].

Rigid polymer foams are versatile engineering materials that find a wide range of applications, mainly as insulators in constructions. Despite the uncorrelated target field, these materials present interesting geometrical properties that could be exploited in a Bragg peak degradation study. Studies have shown that the internal structure presents similarities to the lung parenchyma: a detailed analysis shows $> 90\%$ closed cell content, dimensions of the cells in the order of $\sim 140\mu m$ and binary material composition [32]. However, the density available for rigid polymer foams is limited below $0.1 g/cm^3$, a factor 4 smaller than the lung density. Analogous internal structure but higher densities are found in aerated concrete. In this thesis, a plate of Ytong aerated concrete (Xella GmbH, Duisburg, Germany) is analyzed and used in transmission experiments. The material is shown at the central position in Figure 3.4a and from now on referred as "Phantom C". The nominal density is approximately $0.55 g/cm^3$, slightly above the Phantom A density. Being a copyright protected material, no detailed information is provided regarding the exact elemental composition, which, however, is expected to be close to the nominal concrete composition filled with air cavities. Despite the different composition of Phantom C compared to A and B, the similar internal geometrical structure can provide assess to the capability of the FLUKA MC code to transport charged particles through highly inhomogeneous binary objects.

3.3.2 3D printed phantoms

Parallel to the use of the porous materials, the applicability of 3D printed phantoms is assessed. Check-board phantoms have been the object of interest in previous Bragg peak degradation studies [2]. The design is digitized and then 3D printed with the available Stratasys Objet30 Pro (Stratasys, Eden Prairie, USA), which nominal accuracy is quoted as $16\mu m$ in the vertical direction and $100\mu m$ in the plane normal to it. The material used by the printer is the resin VeroClear RGD810, which nominal polymerized density is $1.19 g/cm^3$. The printing process is based on the deposition of the polymer layer by layer, growing the object in the vertical dimension. Therefore, a voxel filled with solid material can not lay above an air filled voxel, resulting in severe constrains in the randomization of 3D voxel structures. These limitations lead to a preferential use of the printer for the production of regular objects. The results of check-board phantoms with step size $2mm$, $1mm$ and $0.75mm$ are shown in Figure 3.4b. The printer fails to produce phantoms with step size $\leq 0.5mm$ due to uncertainties in the deposition of polymer drops, leading to the pile up of solid and air filled voxels.

Chapter 4

Development of experimental and simulation techniques

In the following chapter the developments necessary to accomplish the systematic study are reported. First, a cumulative approach is studied and implemented in order to separate the physical sources of the Bragg peak degradation. Then, the numerical simulations are refined allowing to reproduce the experiments and obtain comparable outcomes. Finally, an analytic calculation is performed in order to obtain a description of a degraded SOBP under specific circumstances.

4.1 Physical sources of degradation

The degraded Bragg peak is the result of several cumulative effects. To perform a separation one can distinguish the following physical sources of degradation in a inhomogeneous lung-like tissue[1]:

1. Range straggling: intrinsic effect present as well in homogeneous tissues. The scale of the straggling is described by (2.9) and depends on the beam type and initial energy E_0;

2. Scattering: the lateral displacement of beam particles described by (2.11) leads to have particles drifting from tissue-regions with ρ_A to ρ_S and vice-versa, resulting therefore in a different attenuation. The scale of the effect depends on the beam type and on the target geometry;

3. Fluctuations in thickness: in a tissue without ordered structures, at different entrance points and on a straight line in the beam direction, correspond different total quantities of ρ_A and ρ_S material. It results a dependence of (2.4) on the entrance point. The scale of the effect depends on the target geometry.

[1]The lung-like tissue is considered to have randomized internal structures and to be a binary tissue, i.e. composed by two materials with densities ρ_A, ρ_S, in agreement with the description of section 2.2

Table 4.1: List of the cumulative sources, constraints and implementation. The homogeneous phantom refers to a slab of $4.5cm$ of air followed by $4.5cm$ of water. In the randomized phantoms, air cavities are drawn according to the reported geometries. For the check-boards the number of air and water elements in z-direction is fixed $\forall(x, y)$. For the spheres a slight overlap is allowed. $E[\cdot]$ is the expectation value.

Cumulative effects (Naming)	Constraints	Implementation
Sole CSDA (CSDA)	$\sigma_R = 0$ as for (2.9) $WET = \text{const.}, \forall x, y$ No internal structures	Homogeneous phantom Energy straggling disabled
Range straggling (Homogeneous)	$WET = \text{const.}, \forall x, y$ No internal structures	Homogeneous phantom Full physics
Scattering (Check-boards)	$WET = \text{const.}, \forall x, y$ $d = 100\mu m$	Randomized check-boards Full physics
Simple fluctuation thickness ($\sigma^{2D}(WET)$)	$E[WET] = \text{const.}$ $\sigma(WET) > 0$ $d = 100\mu m$	Randomized cylinders Full physics
Complex fluctuation thickness ($\sigma^{3D}(WET)$)	$E[WET] = \text{const.}$ $\sigma(WET) > 0$ d variable ($\sim 100\mu m$)	Randomized spheres Full physics

In a real tissue all the described effects appear in a cumulative way resulting in the total degradation.

4.1.1 Sources separation

In order to separate the physical degradation sources, a cumulative approach is selected. Multiple simulations are performed, starting with the simplest homogeneous phantom until the most complex lung-like phantom. The complexity of the simulation is gradually incremented in a controlled way to include selectively each degradation source. This process is performed by defining a set of constraints for each source, which leads to the definition of a specific simulation. The criterion for the definition of a constraints-set acts as following: when the constraints are fulfilled, the respective source contributes to the degradation together with all the previously listed sources. The list of the sources, constraints and final implementations are reported in the Table 4.1. The NC and MCS are listed together under the scattering effects. The check-board phantoms guarantee that only the scattering effects and the range straggling contribute to the degradation since at every phantom entrance point the WET in the z-direction is constant. Having the approach of a controlled increase in the complexity of the problem, the fluctuations in the thickness are implemented in a two-steps process. The so-called $\sigma^{2D}(WET)$ geometry approximates the alveoli with cylinders having $h \gg r$, following [4]. The more complex $\sigma^{3D}(WET)$ geometry approximates the alveoli with spheres, according to [19].

4.1.2 Implementation algorithms

Each simulation is implemented in FLUKA respecting the required constraints. The implementation of every cumulative effect is given by a specific implementation of the physics and of the phantom geometry.

The sole CSDA requires a specific definition of the physics. Here, the geometry adopted is a homogeneous phantom and it is requested to turn off the energy straggling effects. To do so, a specific card in the FLUKA input is used:

IONFLUCT $-1.$ BLCKHOLE @LASTMAT

Inserting this card, the MC code considers only the average value of (2.3) at every simulation step, setting to zero higher order momenta of the distribution. This is applied for every material in the simulation. In all the other simulations the fluctuations are turned on and the full physics is implemented, i.e. the defaults are set to *precision*.

The separation of the following degradation effects is performed through the selection of a specific phantom-geometry, which are produced using *python* routines that generate directly input files for FLUKA. When necessary, random sampling is performed using the *numpy.random* libraries. The check-boards are generated using infinite intercepting planes to avoid errors in the combinatorial geometry and to allow for a faster tracking. The infinite planes define the regions in the phantom, which are then randomly filled with air or water. In the randomization, care is taken in order to assign the same number of water- and air-filled regions in the z-direction, this is done to assure a fixed water equivalent thickness at every entrance point. The dimension of the rectangular regions in the check-boards is equivalent to the average chord of the cylinders in the following geometry. The $\sigma^{2D}(WET)$ and $\sigma^{3D}(WET)$ geometries are generated by drawing randomized cavities in a water box. To avoid a biased placement of the internal structures, the centers of cylinders and spheres are drawn uniformly over the whole phantom and are included only if the drawn structure does not overlap with an already placed cavity. The air-to-water volume ratio is controlled at every drawn until reaching the desired value. In the $\sigma^{3D}(WET)$ geometry a slight overlap of the spherical cavities is allowed to take in account for the fluctuations in the dimension of the internal structures, two-spheres overlaps are allowed but three-spheres overlaps are avoided. Consequently, the air-to-water volume ratio is updated at every drawn subtracting the volume of the lens resulting from the overlap of two spheres with radius R: $V_{lens} = \frac{1}{12}\pi(4R + d)(2R - d)^2$.

The generation of the randomized phantoms is based on a accept-reject selection, which results in a not-negligible computational time to obtain the desired FLUKA input. The time required increases with the complexity of the geometry and with the air filling of the phantom. For the phantoms with 50% air filling on a single core, one has the following approximate time scales for the generation of the FLUKA input: minutes for check-board, dozens hours for $\sigma^{2D}(WET)$ geometries and several days for $\sigma^{3D}(WET)$ geometries.

4.2 Numerical simulations of the HIT experiments

The systematic study of the Bragg peak degradation is developed through MC simulations. To achieve robust conclusions, an experimental support to the numerical study is performed. The comparison of the numerical and experimental data is only possible after a fine tuning of the MC code in order to closely reproduce the experimental setup and physics. The implementation of the beam and phantom parameters is discussed hereinafter.

4.2.1 Tuning beam parameters

In order to compare the the degraded depth-dose profiles resulting from the experimental and the simulation data, the experimental beam source should be correctly modeled in the MC calculations. To do so, the water reference setup is used. Two different approaches are adopted for ^1p and ^{12}C beams. Moreover, an offset should be assessed for every setup. This is due to the fact that the experimental beam travels through the monitoring system, which gives a specific attenuation and downstream it the entrance chamber of the Peakfinder introduces one more offset. These components are not explicitly modeled in MC and can be practically translated into a water equivalent offset, which results in a rigid shift of the depth-dose in the water tank.

4.2.1.1 ^1p beam

For proton beams, the energy spread introduced by the accelerator and by the monitoring system is modeled with a Gaussian distribution of the momentum of the source particles. The initial momentum of each primary is sampled from a normal distribution centered at the nominal energy and with a specific variance. The Gaussian momentum spread is directly implemented in FLUKA using the BEAM card, which takes $FWHM(p) = 2 \cdot \sqrt{2 \ln 2} \cdot \sigma_p \simeq 2.355 \cdot \sigma_p$ as input parameter. The momentum spread is expected to be in the order of the percent of the total beam nominal momentum. To have an accurate estimator of σ_p and of the offset the following approach is used:

1. multiple simulations of the water reference are performed varying $FWHM^i(p)$ about the expected value;
2. the $80\% - 20\%$ falloff is measured for each simulation (z^i_{80-20}) and for the experimental water reference (z^{exp}_{80-20});
3. $\hat{\sigma}_p$ is extrapolated with a polynomial fit of z^i_{80-20} at varying $FWHM^i(p)$ to meet z^{exp}_{80-20};
4. $\hat{\sigma}_p$ is used to perform one last simulation, which is then adopted to calculate the offset between experiment and simulation. This is given by the difference of the positions at 80% of the falloff: $\Delta_z = z^{exp}_{80} - z^{\hat{\sigma}}_{80}$.

With this work-flow one obtains an estimation of σ_p using the sole fall-off width as parameter, which is independent from Δ_z. The z_{80} is used to estimate the offset since one expects that the range of the primaries corresponds to the 80% fall-off of the Bragg peak [13].

4.2.1.2 ^{12}C beam

For carbon beams, the previously reported approach fails to correctly reproduce the experimental water reference. The introduction of a Gaussian spread in the momentum yields to a correct MC calculation of the fall-off but to an underestimation of the raising flank. The latter has to be interpreted as the result of the mixed particle field, which is generated in the interaction of the primaries with the beam-line. The use of ^{12}C Gaussian distributed in the momentum neglects the presence of lighter particles. To correctly reproduce the experimental results a detailed modeling of the beam-line should be simulated. This has been done in previous works, leading to the generation of a complete phase-space (PS) including the spectrum of primaries and secondaries delivered by the accelerator [33]. The PS is adopted in the simulations of ^{12}C beams. Again, it is necessary to assess the offset between simulation and experimental data since the PS takes in account all beam elements but not the experimental setup. The parameter $\Delta_z = z_{80}^{exp} - z_{80}^{PS}$ is calculated with the same approach as for the proton beam.

4.2.2 Tuning phantom parameters

The phantoms used in the transmission experiments at HIT have to be correctly implemented in FLUKA to assess the MC capability of simulating degraded Bragg peaks. The geometry of the phantoms is generated according to the $\sigma^{2D}(WET)$ model. The implementation of each phantom depends on macroscopic and microscopic parameters, as reported hereinafter.

4.2.2.1 Microscopic: μCT scans, composition

A correct implementation in MC of the phantoms requires a knowledge of microscopic proprieties such as the basic structures and the elemental composition of the solid part.

The internal geometry of the phantoms is analyzed with μCT scans. The highest resolution available is exploited and the voxel side is fixed to $d = 9.6\mu m$. With this setup, the field of view (FOV) is then limited to few centimeters. Therefore, small samples (cubes having $\sim 1cm$ side, Figure 4.1) of the phantom materials are scanned. The small voxel size available allows to correctly resolve the internal geometry. A threshold in the CT values is set assuming a binary model for the materials, i.e. each CT element is assumed to be filled either with air or with solid. The volume ratio air-to-solid (f_A) is then calculated with a dedicated *python* routine, which takes as input the CT data and the threshold, runs through the slides and returns the number of voxels above and below the given threshold. Moreover, a manual contouring is

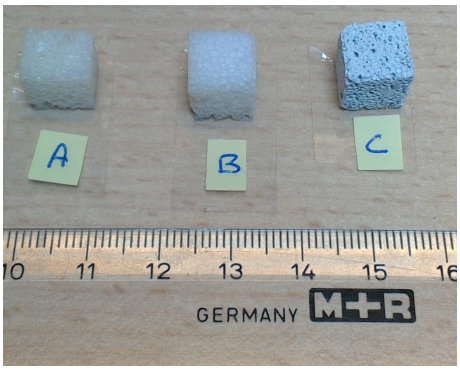

Figure 4.1: Small samples scanned with the μCT. The dimension of the samples is limited by FOV restrictions at the highest resolution.

performed to assess the dimension of the internal structures. In multiple ($n > 10$) slices the air cavities are counted, resulting in the average number of cavities per slice $\bar{N}$. The radius of the cylindrical cavities is then estimated with:

$$\hat{r} = \sqrt{\frac{f_A \cdot A}{\bar{N} \cdot \pi}} \tag{4.1}$$

Were, in (4.1), A is the area of the CT slices and $\hat{r}$ is calculated assuming that the volume fraction f_A corresponds as well to the areal fraction occupied by the section of the cylindrical cavities.

The elemental composition could not be assessed with a direct experiment. Moreover, the materials used are protected by copyright and the explicit atomic compositions are not available. A consistent approximation is therefore used. Maintaining the approach of binary composition, air is assigned to the cavities regions in MC. The solid part is filled with user-defined compounds, which can be directly implemented in FLUKA using the dedicated card COMPOUND together with MAT-PROP to assign the properties. The composition of the solid part of the Gammex phantoms A and B is defined according to [31], where Dual-energy CT was used to investigate Gammex lung properties. Whereas, for phantom C, the standard concrete of the FLUKA libraries is used. The specific composition of the compounds implemented are reported in Table 4.2. The I value is not explicitly set as free parameter but computed by FLUKA according to Seltzer-Berger.

Table 4.2: Elemental composition of the solid part of the phantoms implemented in FLUKA. Composition by weight. Phantoms A, B defined according to [31] and phantom C according to the concrete in the FLUKA libraries.

	H	C	N	O	Mg	Si	Cl	Ca
Phantom A	8.47	59.57	1.97	18.11	11.21	0.58	0.10	0.00
Phantom B	8.47	59.57	1.97	18.11	11.21	0.58	0.10	0.00
Phantom C	10.0	23.0	0.0	40.0	2.0	12.0	0.0	12.0

4.2.2.2 Macroscopic: density, dimension

The macroscopic properties of the phantoms are directly assessed with the use of a precision scale ($\Delta_m = 0.05\,g$) and caliper ($\Delta_x = 0.01\,mm$). Such measurements provide direct access to the total mass (m_{tot}) and total volume (V_{tot}) of the phantoms and, therefore, to the total density ($\rho_{tot} = \frac{m_{tot}}{V_{tot}}$). Theoretically, the density of the solid part can be calculated taking in account the air fraction (f_A) and air density (ρ_A):

$$\rho_S = \frac{\rho_{tot} - \rho_A \cdot f_A}{1 - f_A} \tag{4.2}$$

The MC implementation of the total dimensions and of (4.2) give the strongest dependency on the determination of the WET of the simulated phantom. While the caliper measurement of the z-dimension of the phantom could be considered accurate due to the original design with two parallel faces, ρ_{tot} suffers from the choice of the geometrical model used to to compute V_{tot}. The phantoms used in the transmission experiments at HIT are cut with an electric saw in a cubic shape from larger phantoms. Therefore, the volume is given by $V_{tot} = l_x \cdot l_y \cdot l_z$ in the first approximation, where l_i are the sides dimensions. However, defects in the saw cut (e.g. material missing at the vertexes) result in errors in the computation of V_{tot} and consequently ρ_S, affecting the WET. A more robust approach is adopted to estimate ρ_S and the scale-caliper measurement is used to counter-check the final value.

The density of the solid part of the phantoms is extrapolated from the simulated WET. Experimental and MC depth-dose profiles are aligned according to the offsets obtained while setting the beam parameters. ρ_S is taken as free parameter and varied about the value obtained through the scale-caliper measurements. The estimated $\hat{\rho}_S$ is obtained with a polynomial fit of the position of the simulated Bragg peak 80% falloff with respect to ρ_S to meet the experimental value. With this method ρ_S, f_A, l_z raise from independent measurements providing the correct WET of the phantom.

4.3 Degradation spread out Bragg peak

The special case of degradation independent on the beam properties is developed in order to assess the effect on a spread out Bragg peak.

A SOBP in homogeneous water is the result of the weighted-sum (w_i) of the nominal depth-dose distributions at specific energy steps ($D^{(0)}(z; E_i)$). The resulting dose deposition is given by:

$$D^{(0)}_{\mathrm{SOBP}}(z) = \sum_{i=0}^{n} w_i \cdot D^{(0)}(z; E_i). \tag{4.3}$$

When a SOBP is produced downstream inhomogeneous tissue, in (4.3) the $D^{(0)}(z; E_i)$ should be replaced by $D^{\mathrm{deg}}(z; E_i)$ according to (2.13). The special case of a degradation depending solely on phantom properties and not on the beam energy allows to analytically calculate the depth-dose distribution of a degraded SOBP. To do so, it

should hold:

$$\begin{aligned} \sigma \neq \sigma(E_i) \rightarrow \sigma = const., \forall E_i \\ \mu \neq \mu(E_i) \rightarrow \mu = const., \forall E_i \end{aligned} \tag{4.4}$$

If the (4.4) are respected, then the resulting degraded SOBP can be calculated according to:

$$\begin{aligned} D^{\text{deg}}_{\text{SOBP}}(z) &= \sum_{i=0}^{n} w_i \cdot D^{\text{deg}}(z; E_i) = \\ &= \sum_{i=0}^{n} w_i \cdot \int_{t\in\Omega} dt \cdot D^{(0)}(t; E_i) \cdot \frac{1}{\sqrt{2\pi}\sigma} e^{-\frac{(z-t-\mu)^2}{2\sigma^2}} = \\ &= \int_{t\in\Omega} dt \cdot \sum_{i=0}^{n} w_i \cdot D^{(0)}(t; E_i) \cdot \frac{1}{\sqrt{2\pi}\sigma} e^{-\frac{(z-t-\mu)^2}{2\sigma^2}} = \\ &= \int_{t\in\Omega} dt \cdot \frac{1}{\sqrt{2\pi}\sigma} e^{-\frac{(z-t-\mu)^2}{2\sigma^2}} \cdot \left(\sum_{i=0}^{n} w_i \cdot D^{(0)}(t; E_i) \right) = \\ &= \int_{t\in\Omega} dt \cdot \frac{1}{\sqrt{2\pi}\sigma} e^{-\frac{(z-t-\mu)^2}{2\sigma^2}} \cdot D^{(0)}_{\text{SOBP}}(t) = \\ &= D^{(0)}_{\text{SOBP}}(z) \otimes \mathcal{N}(z \mid \mu, \sigma^2) \end{aligned} \tag{4.5}$$

Where in (4.5) it is possible to exchange the sum over i and the integral over dt due to finite range of sum and integration and not-diverging values of the sum and the integrals. Moreover, the sum inside the integral can be replaced by $D^{(0)}_{\text{SOBP}}(t)$ due to the fact that the (4.4) are respected. Therefore, it results that for degradation parameters independent on the beam properties but solely on the phantom characteristics, the degraded SOBP is the result of the convolution of the nominal SOBP with a Gaussian filter $\mathcal{N}(\mu, \sigma^2)$, where (μ, σ^2) are the same as for the single Bragg peak degradation.

Chapter 5

Experiments and Simulations

In the following chapter the detailed description of the experiments and simulations is reported. The principal objective is to provide a consistent estimation of the parameters' dependencies to be applied in (2.13). The chapter is divided in four sections, structured as follows.

In the first section 5.1 an investigation on the physical sources leading to Bragg peak degradation through MC simulations is performed. The (2.9)-(2.11) and the structure of the lung reported in the section 2.2 are known to cause degradation, however, the specific contributions of each effect have to be assessed.

In the light of the results on the physical sources, in the second section 5.2 a specific model to reproduce lung-like tissue with MC simulations is adopted. The challenging implementation of the complex lung geometry requires a validation through an experimental benchmark, which is here performed.

Assessed the accuracy of the adopted model, in the section 5.3 the dependencies of the (2.13) parameters are investigated. A reference set of parameters is adopted according to Table 2.1, as well as the variability range. Complete dependencies on single parameter variations are assessed. The special case of double parameter variation, inflation and thickness of traversed lung tissue, is investigated for ^1p beams.

Finally in section 5.4 some clinically relevant aspects of the Bragg peak degradation are considered. The effect on a ^1p SOBP is experimentally evaluated, MC simulations are performed in order to asses deviations in LET spectra at the peak position leading to RBE deviations.

5.1 Physical sources of degradation

The first numerical experiment aims to separate the contributions to the final degradation. A simple but effective transmission experiment is used to analyze the shape of the Bragg peak in water downstream lung-like phantoms. The phantoms used do not need to necessarily closely reproduce lung parenchyma, but rather a similar highly inhomogeneous tissue.

5.1.1 Simulation setup

The simulation setup is a simplified implementation of the geometry of a transmission experiment, nevertheless all the relevant structures are introduced. In a transmission experiment the beam is delivered through the phantom and downstream it, i.e. after the sample in the beam direction, the detectors are placed in order to measure the relevant quantities. Here, a water tank is implemented downstream the phantom according to the schematized geometry in Figure 5.1. At the interface between the phantom and the water tank, the energy spectra of primaries and secondaries are scored. In the water tank, the fluence of primaries, secondaries and the dose deposition are scored on a $\Delta z = 0.1mm$ grid in the beam direction. A mono-energetic source, i.e. $p(E)dE = \delta(E_0)dE$, is located upstream the phantom. This is done in order to perform a non-biased estimation of the physical contributions to the degradation: in a real beam one has $\sigma^2(E) > 0$ due to the acceleration process and the presence of the beam control systems, however $\sigma^2(E)$ is facility-dependent. The choice $\sigma^2(E) = 0$ provides a facility-independent result. The same geometrical setup is used for ^1p and

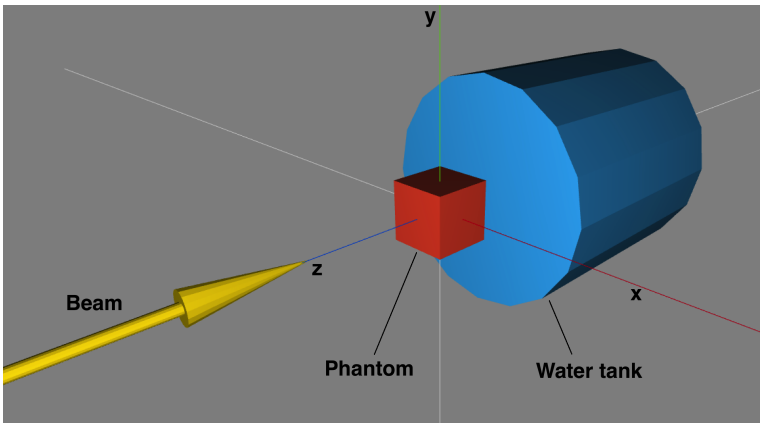

Figure 5.1: Schematic view of a transmission experiment. The beam (yellow) is directed along the z-axis. The phantom (red) is positioned at the isocenter $(0, 0, 0)$. The water scoring volume (blue) lies downstream the phantom. All the structures are centered on the z-axis. View generated with Wings3D.

^{12}C beams. The energies of the beams are set to: $E_0(^1p) = 106.98MeV/u$, $E_0(^{12}C) = 200.28MeV/u$. The used phantoms are generated in order to have a geometry similar to the lung parenchyma, however there is no intent to closely reproduce lung tissue, which is the purpose in section 5.3. The phantoms extend for $l_z = 9cm$ in the z-direction, the volume is filled 50% by water and 50% by air; resulting therefore in $WET = 9cm \cdot \left(0.5 \cdot \hat{S}_{H_2O} + 0.5 \cdot \hat{S}_{air}\right) \simeq 4.5cm$ and similarly $\rho \simeq 0.5g/cm^3$ for every phantom. Where $\hat{S}_i$ are the relative stopping powers of the materials. The dimension of the internal structures is fixed to $d = 100\mu m$. Multiple simulations are performed replacing the phantom according to the methodology presented in Section 4.1. Each simulation is the result of the condensed history of $5 \cdot 10^5$ primary particles.

5.1.2 Range primaries and 80% falloff degraded Bragg peaks

The simulation setup previously described is furthermore adopted to study the accuracy of range calculations for degraded Bragg peaks. Analytical calculations on ^1p beams show how the position having 80% of the maximum dose in the peak falloff corresponds to the range of the primaries [13]. The calculations, however, do not consider degradation effects. A test of the accuracy of z_{80} as range estimator for degraded depth-dose distributions can be performed with the simulation setup reported in Figure 5.1. To do so, the fluence of the primaries is scored in the water tank. The range distribution of the primaries can then be obtained through a numerical derivative:

$$R(z)dz = -\frac{d}{dz}N(z)dz \tag{5.1}$$

The distribution (5.1) is expected to present a Gaussian peak centered at the average range of the primaries. The range position is then projected on the depth-dose distribution to assess the respective position in the falloff.

5.2 $\sigma^{2D}(WET)$ model: experimental benchmark

This second experiment aims to assess the accuracy of the lung-like phantoms used in Section 5.1 in reproducing an experimental degraded Bragg-peak. As previously reported, the complexity of the phantoms implemented in FLUKA may be challenging both in the generation time an as well in the MC simulation time. To perform a degradation-dependencies study, which is the principal objective of this work, a large number of different simulations have to be performed. Therefore a compromise should be accepted between computational time and accuracy in reproducing lung parenchyma degradation. In the light of the remarkable reduction of the generation time and of the acceptable underestimation of the degradation compared to the most complex case, the $\sigma^{2D}(WET)$ model is adopted to reproduce lung parenchyma in FLUKA. The use of cylinders rather than spheres to simulate alveolar structures in MC have been already adopted in previsous studies [4]. To perform a robust experimental benchmark, the beam parameters are tuned on so-called water reference experiments and then used in the setup including the phantom.

5.2.1 Simulation and experimental setups

The simulation setup aims to closely reproduce the transmission experiments performed at the Heidelberg ion-beam treatment center in the experimental room.

The geometry of the simulation is equivalent to the one reported in Figure 5.1. The MC physics is fully implemented, again adopting the *precision* defaults in FLUKA. The beam source is no longer mono-energetic but tuned on the actual experimental beam, the section 4.2.1 is dedicated to this delicate setting. The geometries of the phantoms placed in the front of the water tank are generated according to the $\sigma^{2D}(WET)$ model, where the air-filling is tuned to the specific phantom used. The binary assignation of the materials is maintained. The cavities are filled with air,

whereas the solid regions are filled with user-defined compounds according to the description in section 4.2.2. The water reference experiments refer to the same experimental setup without a phantom upstream the water tank.

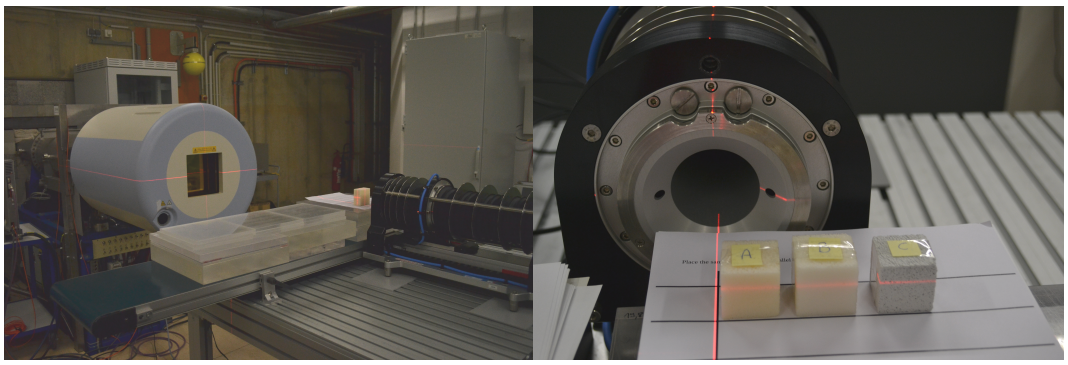

(a) (b)

Figure 5.2: (a) Lateral view of the transmission experiment. The beam is delivered from the treatment head (light-blue and white element) through the phantoms to the Peak Finder. (b) Detailed view of the phantoms placed upstream the Peak Finder. The laser system is used to align the phantoms, which are then moved using the robotic table.

The experimental setup is shown in Figure 5.2. The sole geometrical difference between the experimental and simulation setup is the presence of an air gap between the phantoms and the entrance channel of the Peak Finder, which however is not expected to produce any significant difference in the resulting depth-dose profile measured inside the detector. The phantoms are placed at the isocenter and one of the faces is aligned normal to the beam direction. The use of a printed grid together with the laser system assures a good alignment. The positions of the beam and the detector are fixed, whereas the robotic table where the phantoms are placed can be operated from the control room. The water reference experiments refer to the same experimental setup without any phantoms upstream the water tank, i.e. the robotic table is moved completely laterally. The phantoms A, B and C are irradiated with ^{12}C beam at the energy step E67 ($E_0 = 200.28 MeV/u$), Focus 1 ($FWHM = 4.1mm$) and Intensity 3 on the night-shift between 26.04.2016 and 27.04.2016. The phantom A is irradiated with ^{1}p beam at the energy step E70 ($E_0 = 108.88 MeV/u$), Focus 1 ($FWHM = 14.5mm$) and Intensity 3 on the night-shift between 09.05.2016 and 10.05.2016. No ripple filter is inserted in the beamline. The depth-dose distributions downstream the phantoms are acquired through the dedicated software of the detector. The ^{12}C depth-dose profiles are sampled with a spacing of $\Delta z = 0.05mm$, whereas the ^{1}p ones with a spacing of $\Delta z = 0.25mm$.

5.2.2 3D printed phantoms

An analogous experimental setup is used to assess the degradation downstream the 3D printed check-boards presented in section 3.3.2. The phantoms are irradiated during

the night shift between 06.03.2016 and 07.03.2016. In this case, only the depth-dose distribution of the ^{12}C beam is measured. Again, the beam setting used are energy step E67 ($E_0 = 200.28 MeV/u$), Focus 1 ($FWHM = 4.1mm$) and Intensity 3. No ripple filter is inserted in the beamline.

5.3 $\sigma^{2D}(WET)$ model: degradation dependencies

The third experiment aims to investigate the dependencies of the parameters describing Bragg peak degradation on specific lung properties. To do so, MC simulations are performed adopting the benchmarked $\sigma^{2D}(WET)$ model. In the following, to take in account dimension fluctuations of the internal structures, a slight overlap of the internal structures is allowed, as for the $\sigma^{3D}(WET)$ model. The Bragg peak degradation is described by the convolution model (2.13) with a specific focus on the parameter σ. Multiple beam and lung properties affect the scale of the degradation, the following approach is adopted to perform a systematic analysis: a standard lung treatment is defined fixing to a specific value all the lung and beam parameters and evaluating the related degradation. Then, one per time, every lung and beam parameters are varied about the central value and the change in σ is assessed. Finally, a special case with 2-parameters variations is analyzed. The simulation setup used is a transmission experiment, as reported in Figure 5.1. Again, the lung-like phantoms used have a binary assignation of the materials: air to the cavities and water to the remaining volume. The water implemented in MC simulation allows for variations in density. The study is performed on ^1p and ^{12}C beams.

5.3.1 Standard lung definition

The Bragg peaks downstream lung-like phantoms are parameterized adopting the Gaussian filter model (2.13). While μ refers to the WET of the phantom in the transmission experiment, the degradation is completely described by the parameter σ. Varying the beam type and energy or the microscopic and macroscopic phantom properties, the corresponding Bragg peak degradation and σ vary as well. Therefore, σ depends on multiple lung and beam parameters:

$$\begin{aligned} \sigma &= \sigma(\vec{x}) \\ \vec{x} &= (WET, d, f_A, \rho_S; E_0) \end{aligned} \tag{5.2}$$

Where in (5.2): WET is the water equivalent thickness of the phantom in the transmission simulation, d is the radius of the cylinder in the internal structure of the $\sigma^{2D}(WET)$ phantom, f_A is the volume filling ratio, ρ_S is the density of the solid part of the phantom and E_0 is the energy of the mono-energetic beam used in the simulation. Each given set of variables defines unequivocally a lung-like phantom (e.g. $l_z = WET \cdot (1 - f_A)^{-1} \cdot \rho_S^{-1}$, or $\rho_{tot} = \rho_S \cdot (1 - f_A) + \rho_A \cdot f_A$). A reference set of variables $\vec{x}_0$ is fixed from the data in Table 2.1:

$$\begin{aligned} \vec{x}_0\left(^1p\right) &= \left(2.7cm, 400\mu m, 0.64, 1g/cm^3; 108.88 MeV/u\right) \\ \vec{x}_0\left(^{12}C\right) &= \left(2.7cm, 400\mu m, 0.64, 1g/cm^3; 200.28 MeV/u\right) \end{aligned} \tag{5.3}$$

The phantom parameters of $\vec{x}_0$ reported in (5.3) correspond to a z-dimension $l_z = 7.5cm$ and a total density $\rho_{tot} = 0.34g/cm^3$, within the value ranges of Table 2.1. The dependency on each parameter at the central point can then be assessed with:

$$w_i = \frac{\partial}{\partial x_i}\sigma(\vec{x})\Big|_{\vec{x}_0} \tag{5.4}$$

5.3.2 Single parameter dependencies

Single parameter dependencies are investigated varying one single entry of $\vec{x}$ and fixing the remaining entries to the values in $\vec{x}_0$. For each variation of x_i with $i \in [1, 4]$ a new phantom is generated according to the $\sigma^{2D}(WET)$ model with a dedicated *python* routine. For variations of $x_5 = E_0$ the reference phantom generated with $\vec{x}_0$ is used and the beam source of FLUKA is modified. Each variation of x_i with $i \in \{1, 2, 4, 5\}$ allows to have a consistent generation of a lung parenchyma phantom keeping all the other parameters fixed. On the contrary, the variation of $x_3 = f_A$ is consistent only with a simultaneous variation of d. This is due to the fact that f_A represent the inflation state of the lung parenchyma: assuming a fixed number of alveoli, here implemented as cylinders, $f'_A > f_A$ should correspond to $d' > d$ and viceversa, i.e. the alveoli increase and decrease in size according to the inflation state. A phantom generation considering the sole variation of f_A keeping constant d and consequently varying the number of alveoli would be possible but not realistic. Therefore when changing the inflation state, the phantoms are generated with a dimension of the internal structures:

$$d(f_A) = d^{(0)} \cdot \sqrt{\frac{f_A}{f_A^{(0)}} \cdot \frac{1 - f_A^{(0)}}{1 - f_A}} \tag{5.5}$$

The use of (5.5) allows to maintain a fixed number of alveoli in the phantom.

According to the parameters resulting from previous studies in Table 2.1, the ranges of investigation of x_i are reported in Table 5.1. For an easier interpretation of the values, the last two entries report the variation of the z-dimension of the phantom and the total density relative to the variation of x_1 and x_4.

Table 5.1: Range of investigation of the parameters $\vec{x}$.

x_i	$WET[cm]$	$d[\mu m]$	f_A	$\rho_S[\frac{g}{cm^3}]$	$E_0[\frac{MeV}{u}]$	$l_z[cm]$	$\rho_{tot}[\frac{g}{cm^3}]$
Range	$(.36, 3.6)$	$(200, 500)$	$(.55, .68)$	$(.8, 1.2)$	$(70, 130)\vert_{^1p}$ $(150, 250)\vert_{^{12}C}$	$(1, 10)$	$(.28, .43)$

5.3.3 Interplay air filling and depth

Special attention is given to the simultaneous variation of two lung parameters, which could be particularly relevant for a treatment planning. The interplay effect between the inflation state (x_3) and the depth of the traversed lung parenchyma (x_1) is investigated for ^1p beams. The phantoms are generated on a two-dimensional grid given

by:

$$\vec{x}_0\left({}^1p\right) = \left(x_1, 400\mu m, x_3, 1g/cm^3; 108.88MeV/u\right) \tag{5.6}$$

Due to the two-fold dimension of the problem in (5.6), the variation range of the parameters is here limited to: $x_1 \in (0.9, 2.3)cm$ and $x_3 \in (0.55, 0.65)$.

5.4 Clinical applications

The last series of experiments aims to assess clinical relevant aspects of the degradation effects investigated in the previous analysis. First, the applicability of the Gaussian convolution model is considered in order to reproduce an experimentally degraded proton SOBP. Then, the local effects are investigated in order to explore for possible deviations in RBE due to the variation of the primaries and secondaries energy spectra in a degraded carbon beam.

5.4.1 Experimental degradation ${}^1p$ SOBP

The Gaussian convolution model is expected to successfully reproduce degraded Bragg peaks starting from the nominal water reference and given the phantom properties (WET and σ). In the clinical practice single Bragg peaks undergo a weighted sum in

Table 5.2: Energy steps adopted to generate a ${}^1p$ SOBP. For each energy step the nominal energy, the number of particles and the percentage weight are given.

Energy step	$E_0[MeV]$	n_i	$n_i/\sum_j n_j$ [%]
58	100.46	$2.95 \cdot 10^7$	2.58
61	102.61	$2.24 \cdot 10^7$	1.96
64	104.73	$2.44 \cdot 10^7$	2.13
67	106.82	$2.57 \cdot 10^7$	2.25
70	108.88	$2.66 \cdot 10^7$	2.32
73	110.91	$2.85 \cdot 10^7$	2.49
76	112.91	$2.99 \cdot 10^7$	2.61
79	114.90	$3.24 \cdot 10^7$	2.83
82	116.85	$3.40 \cdot 10^7$	2.98
85	118.78	$3.66 \cdot 10^7$	3.21
88	120.69	$4.04 \cdot 10^7$	3.53
91	122.57	$4.37 \cdot 10^7$	3.81
94	124.44	$4.90 \cdot 10^7$	4.27
97	126.29	$5.37 \cdot 10^7$	4.69
100	128.11	$6.24 \cdot 107$	5.45
103	129.92	$7.75 \cdot 10^7$	6.76
106	131.71	$8.80 \cdot 10^7$	7.68
109	133.48	$1.64 \cdot 10^8$	14.38
112	135.23	$2.75 \cdot 10^8$	24.07

order to generate a SOBP delivering high dose to an extended area. Therefore, the clinical relevant effects of the degradation have to be assesses on a SOBP obtained through a weighted sum of single degraded Bragg peaks. To do so, a transmission experiment with ^1p beam adopting the Phantom A is performed during the night-shift between 09.05.2016 and 10.05.2016. The geometry of the experiment is analogue to Figure 5.2. In order to generate a degraded SOBP, multiple energy steps are irradiated through the phantom and the complete depth-dose distribution in water is acquired at each nominal energy. The Table 5.2 reports the energy steps used in the experiment together with the nominal energy and the number of particles optimized for a plateau dose of $4Gy$. For a better understanding of the values n_i, the last entry of the table reports the relative particles number for each energy step. The energy steps are selected in order to range within typical clinically adopted energies, which lead to generate a SOBP from $8cm$ to $13cm$ of depth in water. The spacing between the energy steps is selected to be $\Delta(E_{step}) = 3$ in order to investigate a clinically applicable SOBP, yet avoiding $\Delta(E_{step}) = 1$ resulting in a extended acquisition time with the Peak Finder. The depth-dose distributions are acquired on a $\Delta_z = 0.5mm$ grid in the z-direction and no ripple filer is inserted in the beam line. The water references at the energy steps $E_{step} = 58$, 70, 112 are acquired in order to tune the beam parameters and obtain through FLUKA reliable water references for each energy step, following the approach described in section 4.2.1. These water references are then used to generate the nominal SOBP, which allows to assess the applicability of the (4.5).

5.4.2 Degradation effect on RBE

The physical effects leading to the Bragg peak degradation, i.e. range straggling (2.9), scattering (2.12) and fluctuations in the thickness, imply a change in the energy spectra of the primary and secondary particles. Such deviations correspond not only to a modified physical dose deposition, but also to a different linear energy transfer (LET) at specific positions and therefore to possible deviations in the relative biological effectiveness (RBE). The biological dose deposited at a given depth is then the combination of the degraded physical dose and the degraded RBE:

$$D^{(0)}_{bio}(z_1) = RBE^{(0)}(z_1) \cdot D^{(0)}(z_1) \;\rightarrow\; D^{\deg}_{bio}(z_1) = RBE^{\deg}(z_1) \cdot D^{\deg}(z_1). \qquad (5.7)$$

To investigate the two-fold dimension of (5.7), a series of MC simulations on a ^{12}C beam are performed. A water reference experiment is compared to a transmission experiment on a lung-like phantom generated according to the definition of the standard lung treatment (5.3) with the geometry reported in Figure 5.1. The simulated beam is mono-energetic with $E_0 = 200.28MeV/u$. The complete LET and energy spectra for primaries and secondaries are scored on a x-y plane at six depths in water: $3cm, 5cm, 7.5cm, 8.5cm, 9.5cm, 14.5cm$. These values are selected in order to analyze specific positions on the nominal water reference Bragg peak: few depths before and after the peak where no significant deviations are expected and few depths in the raising flank, just upstream the peak position and on the distal fall-off where the

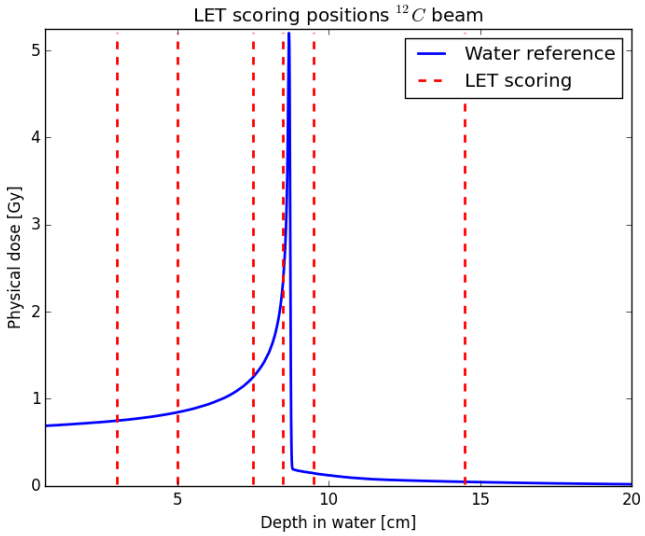

Figure 5.3: Water reference carbon Bragg peak (blue) with the corresponding scoring positions of the energy spectra and LET (red).

largest deviations are expected. The relative positions of the scoring planes and the physical dose deposition of the water reference simulation are shown in Figure 5.3. The same scoring planes are adopted in the MC simulation of the transmission experiment, introducing here a shift according to the water equivalent thickness of the lung-like phantom in order to score the spectra at the correct relative positions on the Bragg peak. The scored spectra and the physical dose distributions are then processed through dedicated algorithms in order to calculate the RBE and the biological dose following the procedure adopted in previsous studies [34]. The RBE data refers to the effect on a generic normal tissue.

Moreover, an analysis of the biological effectiveness of the deposited dose is performed on a fine grid in the z-direction. In this case, the biological effect is assesses through tissue independent physical quantities: the fluence weighted LET and the LET dependent radiation quality factor Q. The first, referred as $fLET$, provides a measurement of the linear energy transfer averaged on the total number of particles depositing dose. For each point in the grid it is calculated according to:

$$fLET(z_1) = \frac{\sum_{i=1}^{N_p(z_1)} LET_i(z_1)}{N_p(z_1)} \tag{5.8}$$

where in (5.8) $LET_i(z_1)$ is the linear energy transfer of the particle i at the depth z_1 and $N_p(z_1)$ is the number of particles depositing energy at the given depth. On the other hand, the radiation quality factor Q is calculated according to the ICRP60 recommendations [35]. This factor aims to characterize the biological effect of the radiation from the ionization density along the tracks of charged particles and it is

calculated according to:

$$Q(LET, z_1) = \begin{cases} 1., & LET(z_1) < 10keV/\mu m \\ 0.32 \cdot LET(z_1) - 2.2, & 10keV/\mu m \leq LET(z_1) \leq 100keV/\mu m \\ 300/\sqrt{LET(z_1)}, & LET(z_1) > 100keV/\mu m \end{cases} . \tag{5.9}$$

The definitions of the quantities (5.8) and (5.9) are tissue independent and rather than assessing the effective biologic response to the radiation, these should be adopted in order to investigate for possible deviations between undegraded and degraded distributions. Such quantities are investigated for a mono-energetic carbon beam with source energy $E_0 = 200.28MeV/u$ and for a carbon SOBP at depths $3.5cm$ to $7.5cm$ in water optimized on the physical dose.

Chapter 6

Results and Discussion

The following sections present the results of the experiments and simulations illustrated in Chapter 5, whose structure is here followed.

6.1 Physical sources of degradation

The depth-dose distributions resulting from MC simulations performed on the phantoms described in Table 4.1 are depicted in Figure 6.1a for the proton beam and in Figure 6.1b for the carbon beam. The plots are normalized to the integral dose. The

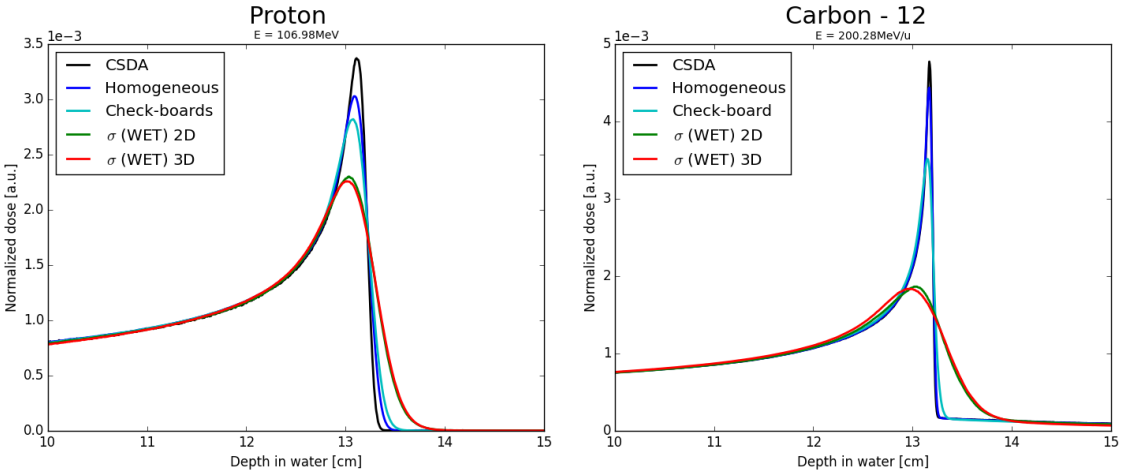

(a) (b)

Figure 6.1: Depth-dose distributions of a proton (a) and a carbon (b) beam downstream lung-like phantoms. The different sources of degradation towards the most complex case are separated.

cumulative approach towards the final degradation is clearly distinguishable in the depth-dose profiles for both ion species: the sharpest Bragg peak is obtained with the sole CSDA, the distributions gradually degrade with the introduction of the range straggling, scattering and finally fluctuations in the thickness. The degradation shows

up in terms of a wider distal falloff (z_{80-20}) and a smaller peak-to-plateau ratio. To perform a robust calculation of the latter, the ratio of the peak dose to the integral dose over a fixed interval of the distribution is computed and then normalized to the value of the CSDA simulation (r_{peak}^{CSDA}) and to the $\sigma^{3D}(WET)$ simulation (r_{peak}^{3D}) for an easier comparison with these extreme values. The numerical results are reported in Table 6.1, where the second entry reports the cumulative percent contribution to the total z_{80-20} degradation. Despite for the natural widening of the Bragg peaks

Table 6.1: Numerical results separation physical sources of degradation, focus on falloff (z_{80-20}) and peak to integral dose ratio (r_{peak}).

Simulation	$z_{80-20}[mm]$	$z_{80-20}[\%]$	r_{peak}^{CSDA}	r_{peak}^{3D}
proton-beam				
CSDA	0.847	30.1	1.0	1.53
Homogeneous	1.26	14.7	0.904	1.38
Check-boards	1.57	11.1	0.887	1.35
$\sigma^{2D}(WET)$	2.68	39.4	0.667	1.02
$\sigma^{3D}(WET)$	2.81	4.7	0.654	1.0
carbon-beam				
CSDA	0.302	7.4	1.0	2.69
Homogeneous	0.372	1.6	0.930	2.50
Check-boards	0.685	7.5	0.732	1.97
$\sigma^{2D}(WET)$	3.84	76.3	0.382	1.03
$\sigma^{3D}(WET)$	4.14	7.2	0.372	1.0

observed with the *homogeneous* simulations, for both ion species the most relevant contribution to the degradation is given by the introduction of the fluctuations in the thickness. This is observed with the highest values of the cumulative percent contribution to the falloff width and with the largest drop in r_{peak}^{CSDA}. The introduction of the most complex fluctuations in the thickness through the $\sigma^{3D}(WET)$ model provide a small, few percent points, extra contribution to the parameters z_{80-20}, r_{peak} compared to the simple fluctuations implemented with the $\sigma^{2D}(WET)$ model. One can conclude that $\sigma(WET)$ of the phantom together with the intrinsic range straggling determine the scale of the degradation and that the scattering effects provide a small contribution. Therefore, lung-like phantoms to be used in degradation studies should include $\sigma(WET)$ and check-board phantoms are not suitable. Detailed considerations regarding the applicability of the check-board phantoms are reported in Appendix A.

The accuracy of the Gaussian convolution model is tested on the degradation of the ^{12}C beam. To do so, the (2.13) is applied choosing the *homogeneous* simulation as $D^{(0)}(z)$. The result of one optimization process is reported in Figure 6.2, where the depth-dose profile resulting from range straggling is convoluted with a Gaussian to fit the depth-dose profile downstream the $\sigma^{3D}(WET)$ phantom. The convolution approach results capable to correctly reproduce a degraded Bragg peak, given the reference one. Again, the most relevant contribution is given by the introduction of the WET fluctuations: from the optimization processes result Gaussian filters with

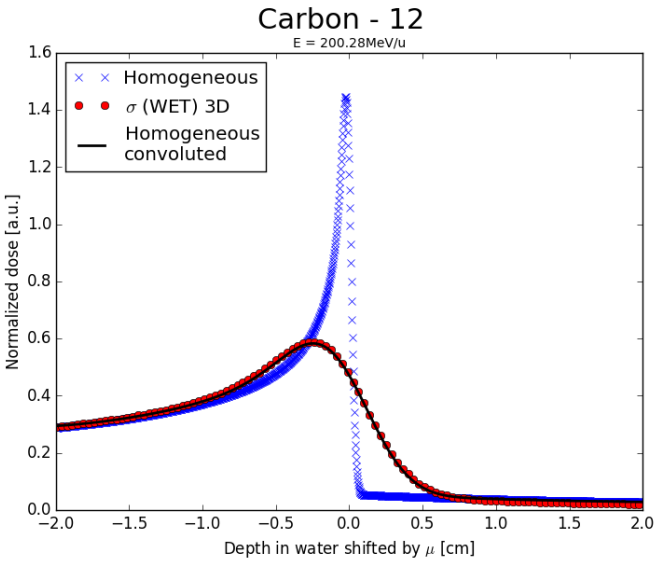

Figure 6.2: Gaussian convolution model to reproduce Bragg peak degradation. The fit (black line) of the $\sigma^{3D}(WET)$ degraded curve (red circles) is obtained with a convolution of the water reference (blue crosses) with $\mathcal{N}(x \mid \mu = 0mm, \sigma = 2.60mm)$

$\sigma = 0.39mm$ when considering the scattering effects, $\sigma = 2.39mm$ when introducing the simple fluctuations and finally $\sigma = 2.60mm$ when considering the most complex case.

In the light of the results obtained dividing the physical sources of degradation, the $\sigma^{2D}(WET)$ model is adopted as reference phantom to reproduce static lung parenchyma. The underestimation of the degradation compared to the most complex case is moderate (few percent effects in z_{80-20} and r_{peak}) and is therefore accepted as compromise with the reduced computation time.

6.1.1 Range primaries and 80% falloff degraded Bragg peaks

The range of the primaries ($\hat{R}$) is obtained from multiple simulations with a Gaussian fit of the distribution (5.1). The dose at the falloff position corresponding to the range is then normalized to the peak dose ($\frac{D(\hat{R})}{D_{max}}$). The results reported in Table 6.2 show that also for degraded Bragg peaks holds that the range of the primaries corresponds to a dose value about the 80% of the peak dose. To justify the use of z_{80} as range estimator, an error calculation is performed. The last entry of the table reports the percentage error committed when estimating the range of the primaries with z_{80} instead of using the real value $\hat{R}$. This approach is commonly used in physical experiments, where the particle fluence here obtained with MC is not available. For both ion species the $err_{80\%}$ results limited to $\sim 1‰$.

6.2 $\sigma^{2D}(WET)$ model: experimental benchmark

6.2.1 Experimental data

The depth-dose distributions normalized to the entrance channel, as standard output from Peakfinder experiments, acquired during the experiments at HIT are reported in Figure 6.3a for the proton beam and in Figure 6.3b for the carbon beam. Due to time

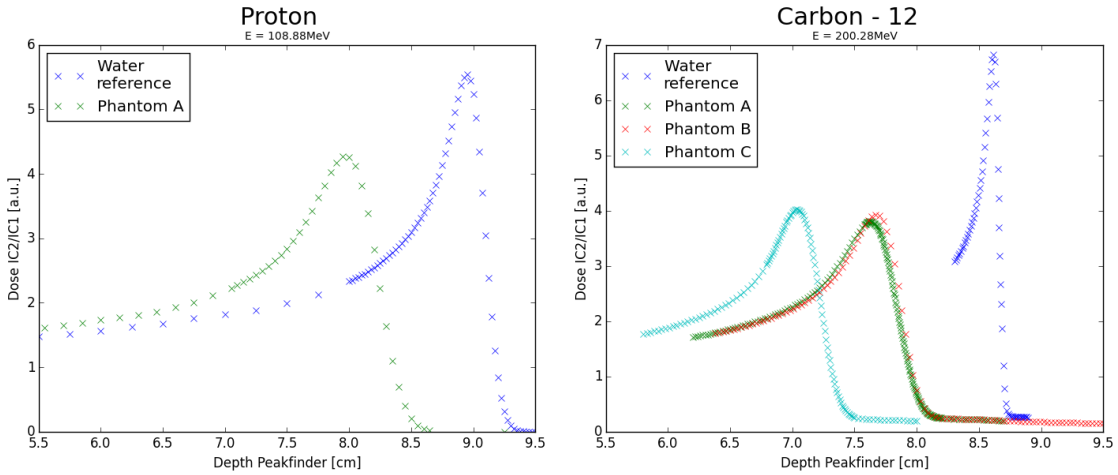

(a) (b)

Figure 6.3: (a) Experimental data transmission experiment Phantom A and water reference proton beam. (b) Experimental data transmission experiment Phantoms A, B, C and water reference carbon beam.

limitations, the scan of the degraded carbon Bragg peak downstream the Phantom B has been performed with a 6 times reduced resolution, resulting in spacing between the data points $\Delta_z = 0.3mm$. The data allows to extract degradation parameters as

Table 6.2: Primaries range estimation and comparison with 80% falloff position.

Phantom	$\hat{R}[cm]$	$\frac{D(\hat{R})}{D_{max}}[\%]$	$err_{80\%}[\%]$
proton-beam			
Homogeneous	13.18	80.41	$-7.8 \cdot 10^{-3}$
Check-boards	13.18	80.48	$-1.1 \cdot 10^{-2}$
$\sigma^{2D}(WET)$	13.20	81.18	$-3.9 \cdot 10^{-2}$
$\sigma^{3D}(WET)$	13.20	80.97	$-3.6 \cdot 10^{-2}$
carbon-beam			
Homogeneous	13.19	78.74	$+6.0 \cdot 10^{-3}$
Check-boards	13.19	81.22	$-9.8 \cdot 10^{-3}$
$\sigma^{2D}(WET)$	13.21	82.87	-0.11
$\sigma^{3D}(WET)$	13.20	82.11	-0.10

for the analysis performed on the MC simulations in the section 6.1. The results are reported in Table 6.3. Here, it is not possible to perform a robust estimation of the

Table 6.3: Bragg peak degradation parameters extracted from the transmission experiments at HIT.

Experiment	$z_{80-20}[mm]$	$WET[cm]$	$\sigma[mm]$
proton-beam			
Water reference	1.37	0.0	0.0
Phantom A	2.31	0.89	1.47
carbon-beam			
Water reference	0.465	0.0	0.0
Phantom A	2.13	0.87	1.44
Phantom B	1.84	0.84	1.30
Phantom C	1.81	1.48	1.21

peak to integral dose due to the limited scanned range of the water reference. As well, the peak to entrance dose ratio would not be consistent due to the different WET of the phantoms. Therefore, the degradation parameters reported are the distal falloff z_{80-20} and the Gaussian convolution parameter σ, together with the WET of the phantoms. From the data reported in the Table 6.3 once can notice how the sharper falloff in water for ^{12}C beam compared to ^{1}p beam (~ 3 times larger z_{80-20}) reduces to a comparable value downstream the Phantom A. Moreover, the Gaussian σ appears to be independent from the particle type, resulting in deviations up to 1% about the average value $\bar{\sigma} = 1.455mm$. Such deviations may be justified by a different shooting position through the Phantom A during the two night-shifts, hypothesis supported by small a fluctuation observed as well in the water equivalent thickness.

6.2.2 Tuning beam parameters

For the proton beam, the method described in the section 4.2.1 is applied. At the variation of the Gaussian width of the source momentum corresponds a widening of the distal falloff as plotted in Figure 6.4. A quadratic fit is performed to extrapolate the value leading to the experimentally observed falloff. This is then used to evaluate the WET offset between the simulation and the experiment, using the 80% falloff. It results:

$$\begin{aligned} FWHM(p) &= 1.61 \cdot 10^{-3}\, GeV \\ \sigma(p) &= 6.84 \cdot 10^{-4}\, GeV \\ \Delta_z &= -0.0833\, cm. \end{aligned} \tag{6.1}$$

The values (6.1) lead to the definition of the simulation parameters adopted for the benchmark study. The resulting simulated Bragg peak, compared to the experimental one, is plotted in Figure 6.5a. The method leads to an excellent agreement between MC and the HIT data. A Gaussian distribution of the ^{1}p momenta is therefore sufficient to perform the benchmark study without implementing a more complex phase space.

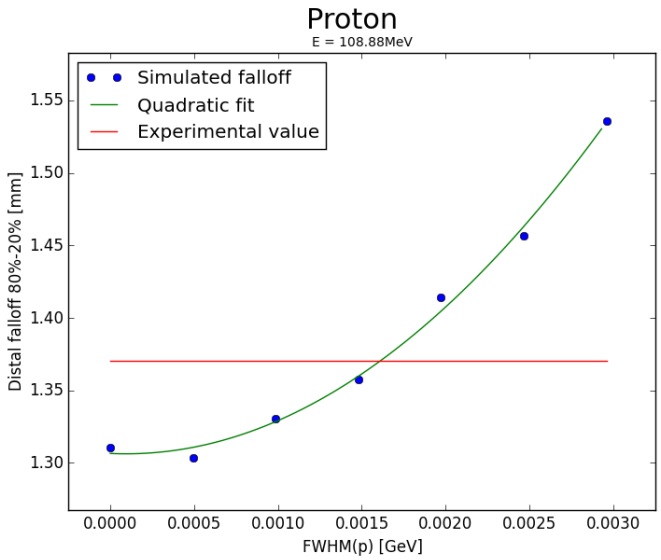

Figure 6.4: Quadratic dependence of the simulated distal falloff of a proton beam (blue simulations, green quadratic interpolation) compared to the experimental value (red)

For the carbon beam, the previously adopted method fails to reproduce the experimental Bragg peak with high agreement in all its components. A more sophisticated approach is therefore adopted by simulating the complete PS delivered by the beam nozzle [33]. The results are plotted in Figure 6.5b where, for comparison, multiple possible methods are reported. The light blue curve is the result of a monoenergetic source resulting in an underestimation both of the distal falloff and the raising flank. The red curve is the result of the method previously applied to the ^1p beam. In this case the distal falloff is properly reproduced, being the free parameter of the fit, but the raising part of the peak is underestimated. The best result is obtained with the use of the complete phase space, shown in green. Nonetheless a slight underestimation of the raising flank is observed, which may be attributed to the accuracy of the nuclear interaction models for ^{12}C in the FLUKA code. The PS simulation is adopted for the benchmark study with the resulting offset from the experiment of $\Delta_z = +0.0815cm$. The latter should be compared to the respective value obtained for protons 6.5a observing that for the ^{12}C beam the BAMS has been modeled in the PS, whereas for the ^1p beam the Gaussian distribution of the momenta does not take in account the monitoring system. The absolute difference between the two offsets is compatible with the value $WET(BAMS) = 160\mu m$ reported in the literature [24].

Both for the carbon and the proton beams the output of the simulations is given in deposited dose per primary particle. The experimental output returns the ratio between the IC2 to IC1 readout. Here, one is interested in reproducing the shape and the relative parameters of the Bragg peaks (e.g. z_{80-20}, σ) and not to absolute values (e.g. dose deposited at the peak position). Therefore a robust definition of a conversion factor is not required. The estimations and the plots in Figure 6.5a and 6.5b are obtained with a normalization to 1 at the peak maximum.

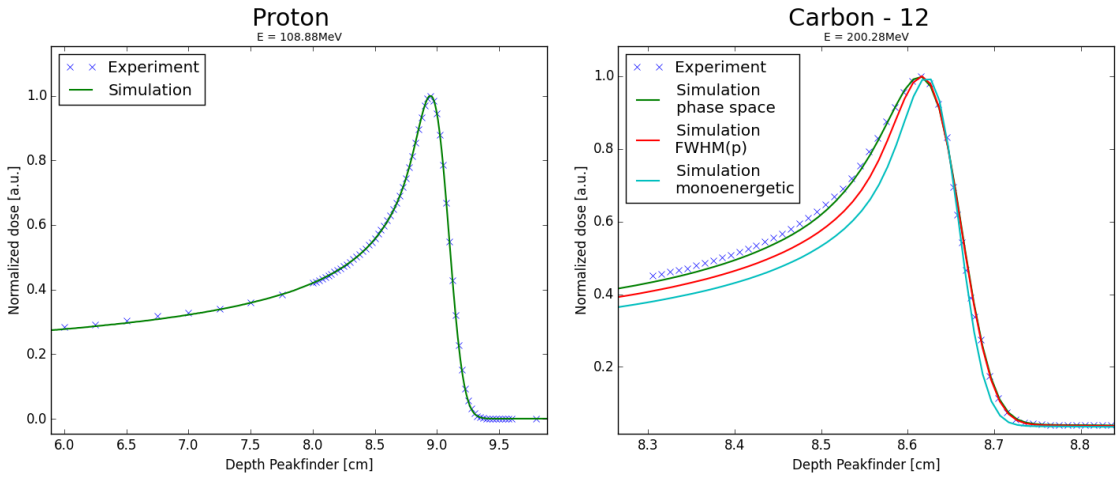

(a) (b)

Figure 6.5: (a) Comparison of the experimental (blue crosses) and the simulated (green) water reference for a proton beam with the parameters (6.1). (b) Comparison of the experimental (blue crosses) and the simulated water reference for a carbon beam. The resulting curves from a monoenergetic beam (light blue), Gaussian spread in the momentum (red) and phase space source (green) are shown.

6.2.3 Tuning phantom parameters

The Figure 6.6 shows three cropped slices of the phantoms resulting from the μCT scans at the smallest voxels size available ($d = 9.6\mu m$). Despite the different composition of the solid part and varying air filling, the micro tomography of Phantom C shows, as expected, a similar internal geometrical structure to the Gammex phantoms. Each μCT DICOM image results in data-weights in the order of $10GB$, impossible to directly implement in FLUKA through the DICOM import module also due to specific requirements of the software oriented towards patient CT scans rather than μCT scans (e.g. the outer CT layer should be air). The scans were performed during the night between 01.06.2016 and 02.06.2016 due to the long time required to perform all the projections and obtain the maximum resolution. The scan of the Phantom B suffered from a misalignment error with a small portion of the phantom outside the field of view, resulting in severe artifacts as observed in Figure 6.6b. The presence of artifacts leads to high uncertainties in the results of the *python* routine used to estimate f_A. This, together with the reduced resolution in the Bragg peak data in Frigure 6.3b, suggests to leave out from the benchmark study the Phantom B; decision supported by the fact that the Phantom A itself provides information on the degradation due to Gammex lung-like material. The different air filling of Phantom A and Phantom C is directly noticeable from the CT histograms in Figure 6.7, where the left peaks have to be associated with the volume occupied by air and the counts at higher values with the volume occupied by solid material. The chosen thresholds are respectively $th(A) = 4500$ and $th(C) = 2000$, which return the air filling values over the whole DICOM image. The dimension of the internal structures is estimated

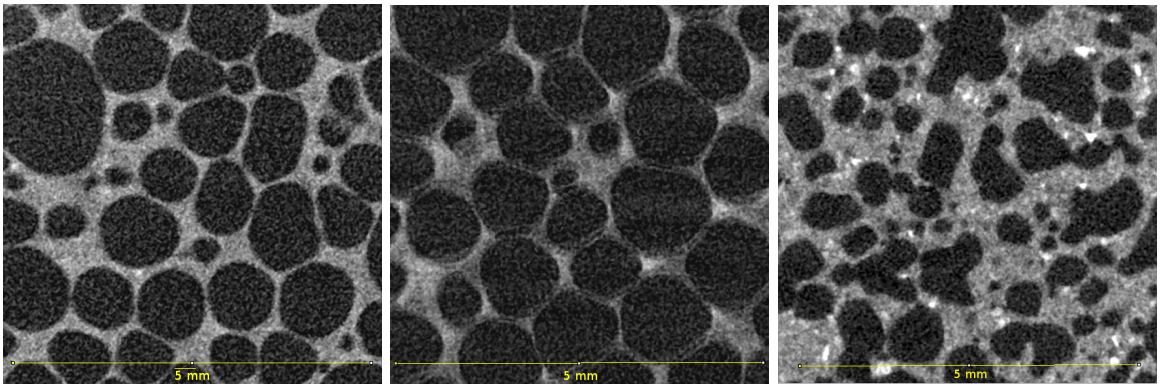

(a) (b) (c)

Figure 6.6: Cropped views of three slices resulting from the μCT scans of Phantom A (a), Phantom B (b) and Phantom C (c). Scale provided at the bottom of the images.

Table 6.4: Estimated parameters Phantom A and Phantom C.

Parameter	Phantom A	Phantom C
f_A	0.73	0.45
$\hat{r}[\mu m]$	469	316
$\rho_S^{WET}[g/cm^3]$	1.16	1.04
$\rho_S^{Scale}[g/cm^3]$	1.04	1.05
$l_z[cm]$	3.000	3.043

according to (4.1). The z-dimension and ρ_S^{Scale} are measured with the caliper-scale method according to (4.2). Whereas, ρ_S^{WET} is estimated through the water equivalent thickness of the phantom considering the appropriate Δ_z measured in the previous section. All the phantom parameters are reported in Table 6.4. The parameter ρ_S^{WET} is adopted to perform the benchmark, while the comparison with ρ_S^{Scale} shows that the scale-caliper method is affected by an intrinsic uncertainty due to the calculation of the phantom volume. Nonetheless, the latter provides a counter-check on the approximate value of ρ_S eventually adopted.

6.2.4 Monte Carlo benchmark

The resulting comparison of the FLUKA simulations performed with the beam parameters described in section 6.2.2 and the phantom parameters of Table 6.4 is shown in Figure 6.8. The simulation output is normalized to the experimental data, i.e. the absolute dose per primary is converted into $IC2/IC1$. Good agreement of the MC simulations is observed, especially for the transmission experiment with Phantom A with the proton beam and Phantom C with the carbon beam. A slight underestimation of the degradation is expected due to the adoption of the $\sigma^{2D}(WET)$ to reproduce the phantom geometry. Nonetheless, the relevant properties of the degraded Bragg peaks are correctly reproduced, including a smaller peak to plateau ratio and a wider

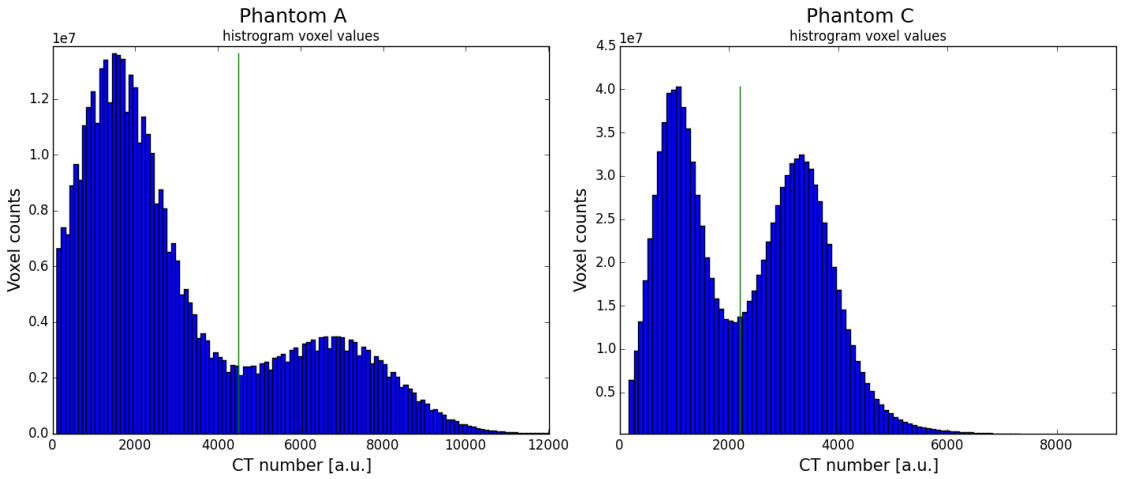

(a) (b)

Figure 6.7: Histograms of the CT numbers resulting from the μCT scan of the Phantom A (a) and Phantom C (b). The green line shows the threshold selected.

distal falloff. The degradation parameters resulting from the MC simulations are reported in Table 6.5. Where the entries u_i [%] are the percentage underestimation

Table 6.5: Estimated degradation parameters for the MC simulations of Phantom A and Phantom C. The entries u_i report the percentage comparison with the experimental values of Table 6.3.

Simulation	$z_{80-20}[mm]$	$u_{z_{8020}}$ [%]	$\sigma[mm]$	u_σ [%]
Phantom A (^1p)	2.21	95.7	1.33	90.5
Phantom A (^{12}C)	1.98	93.0	1.33	92.4
Phantom C (^{12}C)	1.79	98.9	1.20	99.2

values of the degradation obtained through the MC implementation compared with the experimental values of table 6.3. The $\sigma^{2D}(WET)$ model underestimates the distal falloff up to 5% and the Gaussian σ up to 10% compared to the experimental values for Phantom A. Just a slight underestimation is observed for Phantom C ($\sim$ 1%). Moreover, there is a complete agreement between carbon and proton beams on the σ downstream the Phantom A. Contrary to the experimental case, in the simulation the proton and carbon beams travel through the identical phantoms with the same entrance point, suggesting that the Gaussian σ is independent on the beam particle and depends solely on the phantom properties.

Despite the expected and observed underestimation of the parameters, the $\sigma^{2D}(WET)$ model is capable to reproduce the characteristics of degraded Bragg peaks due to inhomogeneous phantoms. It is capable not only to reproduce the specific degradation of one specific lung-like material, but also the different behavior downstream phantom presenting varying ρ_S, f_A and material properties. For these reasons, the $\sigma^{2D}(WET)$ model is adopted to study the dependencies of σ on lung parameters.

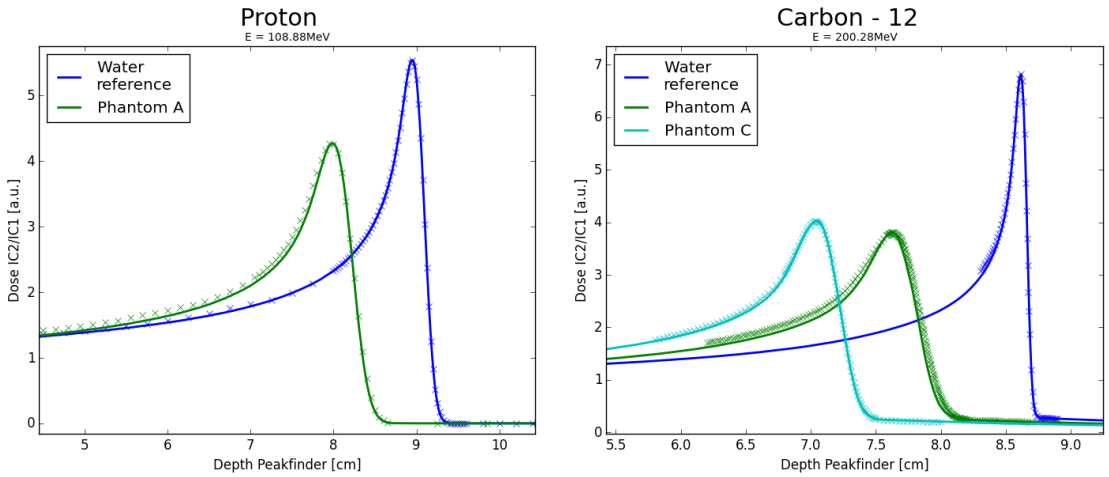

(a) (b)

Figure 6.8: Outcome of the experimental benchmark of the MC simulation adopting the $\sigma^{2D}(WET)$ to simulate Phantom A and C.

6.2.5 3D printed phantoms

The Figure 6.9 shows the internal structure of the 3D printed check-board phantom with step size $d = 750\mu m$. The axial view shows how the elements designed in

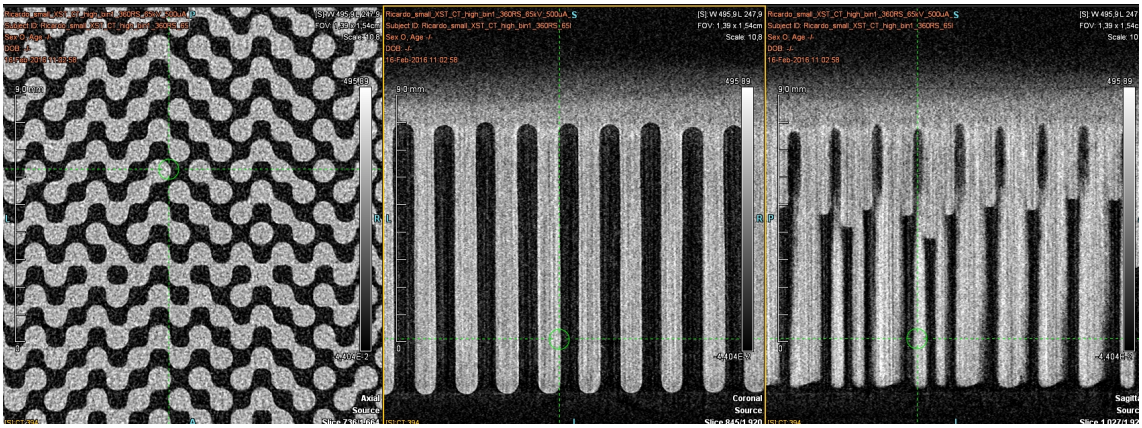

Figure 6.9: From the left to the right: axial, coronal and sagittal plane of the micro tomography performed on the 3D printed check-board phantom with step size $d = 750\mu m$.

a rectangular shape are then produced with a circular section. According to the original design the elements should be intercepting only on a line along one corner; in the printed phantom the cylindrical-like elements randomly present an extended connection with the neighbors. Moreover, the sagittal view reveals the presence of material dropped in the regions originally designed as air cavities. These printing defects are observed also in the phantoms having larger step-size.

The use of unrealistic check-board phantoms to reproduce lung tissue is useful to provide physical information due to the well defined geometry, such as in the simulations presented in the section 6.1. The printing errors affect the knowledge of the exact geometry. As a matter of fact, the experimental results of the transmission experiments through the 3D printed phantoms present a total disagreement with the corresponding MC simulation having the originally designed geometry implemented. Therefore, 3D printed objects are left out from the degradation study.

6.3 $\sigma^{2D}(WET)$ model: degradation dependencies

6.3.1 Single parameter dependencies

The dependencies of the Gaussian σ describing the Bragg peak degradation over the parameters (5.2) about the central point (5.3) and in the ranges reported in Table 5.1 are reported in Figure 6.10 for the proton beams and in Figure 6.11 for the carbon beams. The functions adopted to fit the data points are selected without any specific

Table 6.6: Numerical results of the MC study on the dependencies on single parameter variations. The coefficients of the fit a_i are reported together with the first order derivatives w_i at the reference value according to (5.4).

Parameter	Fit function	a_i	w_i
proton-beam			
$x_1 = WET$	$\sigma(x_1) = a_1 \cdot \sqrt{x_1}$	$a_1 = 1.43\,\frac{mm}{\sqrt{cm}}$	$0.435\,\frac{mm}{cm}$
$x_2 = d$	$\sigma(x_2) = a_2^{(0)} + a_2^{(1)} \cdot x_2$	$a_2^{(0)} = 3.3 \cdot 10^{-3}\,\frac{mm}{\mu m}$ $a_2^{(1)} = 0.96\,mm$	$3.3 \cdot 10^{-3}\,\frac{mm}{\mu m}$
$x_3 = f_A$	$\sigma(x_3) = a_3 \cdot x_3$	$a_3 = 3.67\,mm$	$3.67\,mm$
$x_4 = \rho_S$	$\sigma(x_4) = a_4 \cdot x_4$	$a_4 = 2.32\,\frac{mm \cdot cm^3}{g}$	$2.32\,\frac{mm \cdot cm^3}{g}$
$x_5 = E_0$	$\sigma(x_5) = a_5$	$a_5 = 2.32\,\frac{mm \cdot u}{MeV}$	0.
carbon-beam			
$x_1 = WET$	$\sigma(x_1) = a_1 \cdot \sqrt{x_1}$	$a_1 = 1.43\,\frac{mm}{\sqrt{cm}}$	$0.435\,\frac{mm}{cm}$
$x_2 = d$	$\sigma(x_2) = a_2^{(0)} + a_2^{(1)} \cdot x_2$	$a_2^{(0)} = 2.8 \cdot 10^{-3}\,\frac{mm}{\mu m}$ $a_2^{(1)} = 1.1\,mm$	$2.8 \cdot 10^{-3}\,\frac{mm}{\mu m}$
$x_3 = f_A$	$\sigma(x_3) = a_3 \cdot x_3$	$a_3 = 3.62\,mm$	$3.62\,mm$
$x_4 = \rho_S$	$\sigma(x_4) = a_4 \cdot x_4$	$a_4 = 2.13\,\frac{mm \cdot cm^3}{g}$	$2.13\,\frac{mm \cdot cm^3}{g}$
$x_5 = E_0$	$\sigma(x_5) = a_5$	$a_5 = 2.25\,\frac{mm \cdot u}{MeV}$	0.

association to a model, but according to dependencies consistent with the data and to the tendency expected. In particular, the functions describing $\sigma(x_1)$, $\sigma(x_3)$ and $\sigma(x_4)$ should be consistent with $\sigma \to 0$ for $x_1, x_3, x_4 \to 0$ due to the fact that for a zero-value of the parameters x_i the transmission experiment should reduce to a water reference simulation. The variation of x_5 do not show any significant dependence of the degradation on the parameter and therefore a constant fit function is adopted.

The absence of a dependency $\sigma(E_0)$ can be interpreted as for σ being dependent solely on the phantom parameters and not on the beam type or energy. No specific behavior or tendency is expected for $x_2 \to 0$ or $x_2 \to +\infty$ and therefore a constant fit is adopted, but a more accurate analysis of the residuals suggests the use of a linear fit function introducing one more parameter. Therefore, a statistical test based on the F distribution is performed [36]. It results that a linear fit with two parameters is more significant, rejecting the $\sigma(x_2) = a_2$ hypothesis with a confidence level $p < 0.005$ for both ion species. The rejected hypothesis is plotted with a dashed line.

The fit functions used, the numerical results and the corresponding calculation of the (5.4) for every x_i are reported in Table 6.6. The accuracy of the method is assessed by performing multiple ($n > 10$) generations of $\sigma^{2D}(WET)$ phantoms with fixed $\vec{x}_0$, simulating the transmission experiment and evaluating the fluctuation of the σ. It results that measured and predicted data points should be considered having a relative error:

$$\frac{\Delta\sigma(\vec{x})}{\sigma(\vec{x})} = 0.0251 = 2.51\% \tag{6.2}$$

The value (6.2) is reported with absolute error bars in Figure 6.10 and in Figure 6.11.

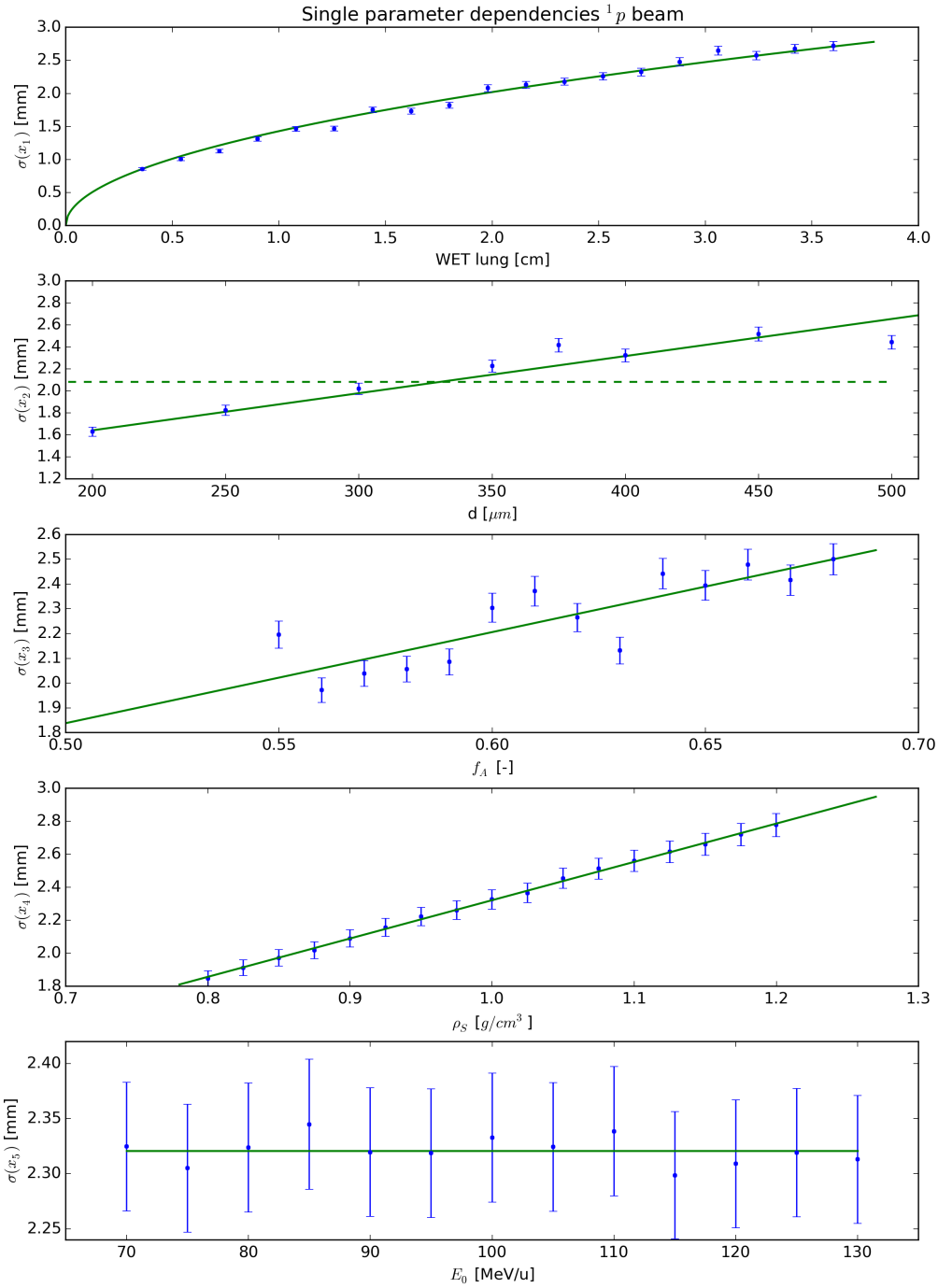

Figure 6.10: Gaussian σ for proton beam. Dependencies on the x_i parameters: WET, d, f_A, ρ_S, E_0. MC simulations (blue dots) fitted with the corresponding curve (green). The scale for σ is not constant.

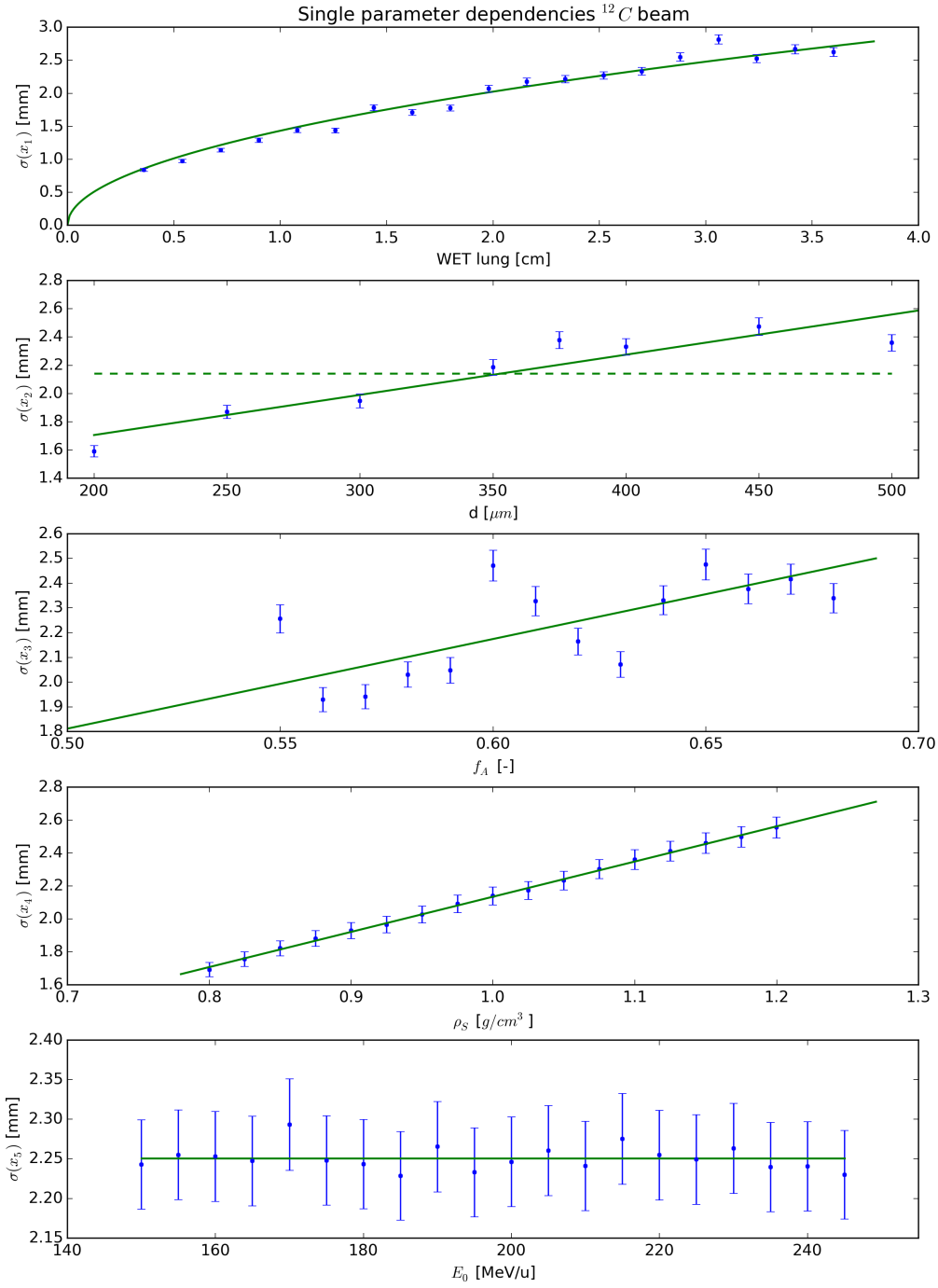

Figure 6.11: Gaussian σ for carbon beam. Dependencies on the x_i parameters: WET, d, f_A, ρ_S, E_0. MC simulations (blue dots) fitted with the corresponding curve (green). The scale for σ is not constant.

6.3.2 Interplay air filling and depth

The Bragg peak degradation resulting from the two parameters variation on the grid defined by (5.6) is reported in Figure 6.12. The data points are interpolated accord-

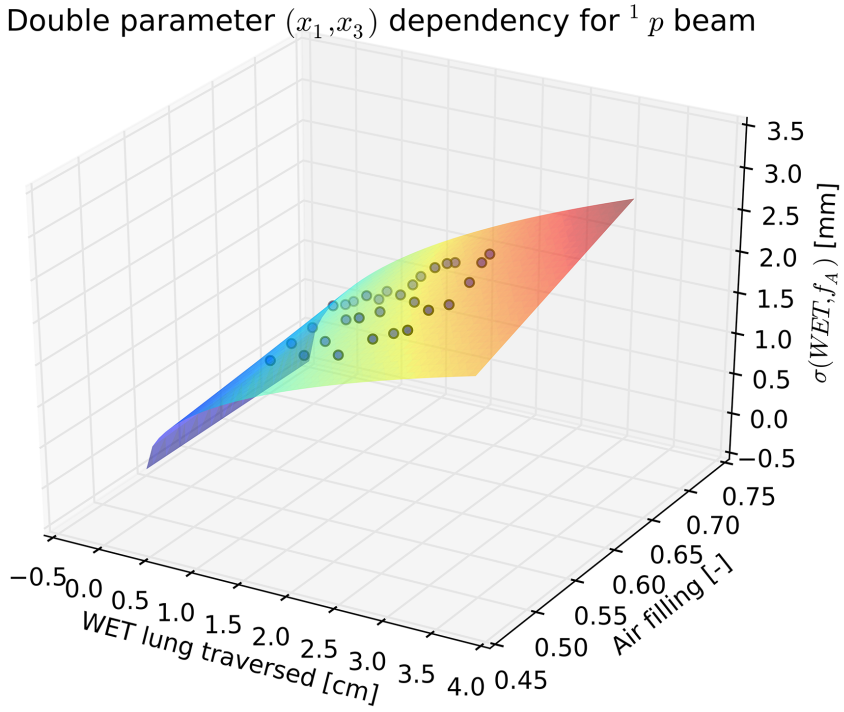

Figure 6.12: Gaussian σ for proton beam. Dependencies on x_1 and x_3 parameters. MC simulations (blue dots) fitted with the two-dimensional function (6.5).

ing to linear combinations of the functions $\sigma(x_i)$ adopted for the single parameter dependencies. A statistical analysis is performed on the functions:

$$\begin{aligned} f_1(x_1, x_3) &= a \cdot \sigma(x_1) + b \cdot \sigma(x_3) + c \cdot \sigma(x_1) \cdot \sigma(x_3) \\ f_2(x_1, x_3) &= a \cdot \sigma(x_1) + c \cdot \sigma(x_1) \cdot \sigma(x_3) \\ f_3(x_1, x_3) &= c \cdot \sigma(x_1) \cdot \sigma(x_3) \end{aligned} \tag{6.3}$$

where in (6.3) each step $f_i \to f_{i+1}$ is performed by removing the least significative contribution to f_i according to the p-value of the t-test. The resulting values of the Bayesian information criterion (BIC) for the f_i are:

$$\begin{aligned} BIC(f_1) &= -194.24 \\ BIC(f_2) &= -197.49 \\ BIC(f_3) &= -198.58. \end{aligned} \tag{6.4}$$

The results (6.4) suggest that the most relevant contribution to the fit function is given by the term $\sigma(x_1) \cdot \sigma(x_3)$, which then allows to interpolate the data points with

a fluctuations of the residuals about 4%. Therefore, the function f_3 is adopted to fit the data in Figure 6.12 with the coefficient resulting from the interpolation:

$$f_3(x_1, x_3) = 2.21 \cdot x_3 \cdot \sqrt{x_1}. \tag{6.5}$$

The (6.5) can then be used to predict the results of the degradation observed in the section 6.1 using as input parameters $x_1 = 4.5cm$, $x_3 = 0.5$ and obtaining $\sigma = 2.34mm$, which is compatible with the previously observed value $\sigma = 2.39mm$ within the relative error (6.2) assessed for the method.

6.4 Clinical applications

6.4.1 Experimental degradation ^1p SOBP

The experimental data of the dose deposition for multiple ^1p beams downstream the Phantom A and the corresponding simulations of the water references at the energies reported in Table 5.2 are plotted in Figure 6.13. The simulated water references

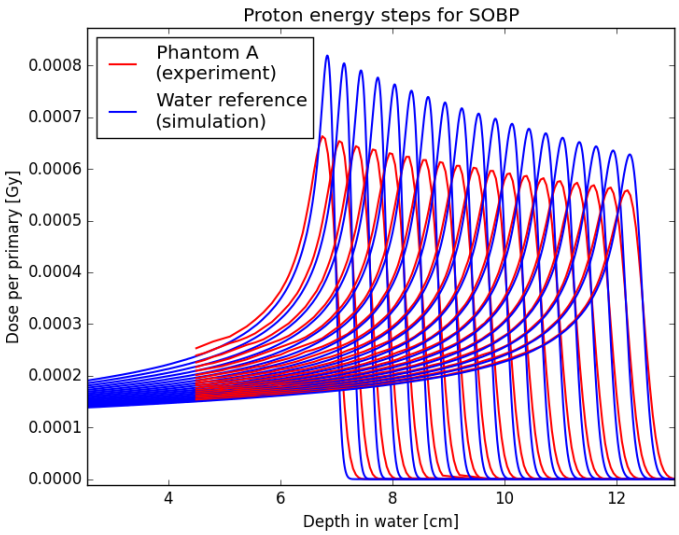

Figure 6.13: Energy steps of the ^1p beam used to produce a SOBP. The experimental data downstream the Phantom A (red) is normalized to the unit of the water reference simulation data (blue).

are shifted by the WET of the phantom in order to be directly compared with the degraded Bragg peaks at the same energy. Moreover, it is here necessary to perform a robust normalization of the $IC2/IC1$ output of the Peak Finder. This is due to the fact that to obtain a SOBP, the absolute dose has to be summed through the respective weights and the previously adopted normalizations to the dose-maximum or to the integral-dose are meaningful to compare Bragg peaks at the same energy step but not to add the deposited dose at different energy steps. To do so, the integral on a fixed Δ interval about z_{80}, and therefore about the mean range of the

primaries, is calculated for every peak in Figure 6.13. The resulting normalization coefficient for the experimental data is then given by the ratio of the simulation to the experimental integral, at each energy step. The $IC2/IC1$ readout is, with this approach, normalized to the unit of the simulation data, i.e. deposited dose per primary particle. The normalized depth-dose distribution shown in Figure 6.13 can then undergo the weighted-sum (4.3).

The results of the weighted-sums are shown in Figure 6.14 and, moreover, with a focus on the plateau and the tail regions in Figure 6.15. The water reference

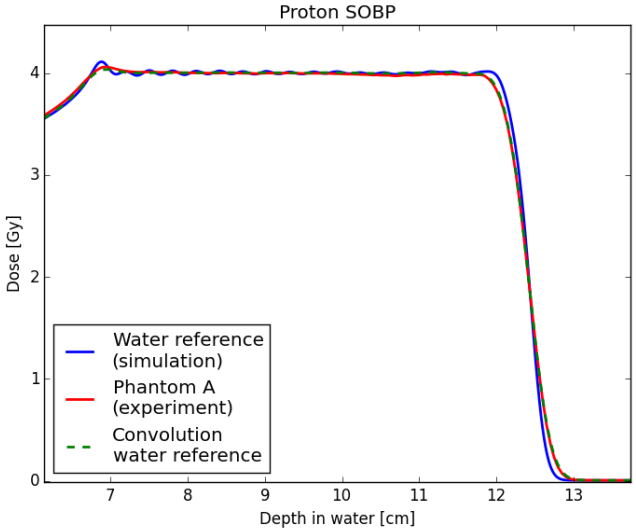

Figure 6.14: Resulting proton SOBP with weighting according to Table 5.2. The water reference SOBP (blue) is convoluted with a Gaussian $\mathcal{N}(\mu = 0., \sigma = 1.47mm)$ (green) and compared to the experimental degraded SOBP (red).

SOBP is convoluted with a Gaussian $\mathcal{N}(\mu = 0., \sigma = 1.47mm)$ to obtain the degraded SOBP according to the result of (4.5). The adopted value of σ is the one previously reported in Table 6.3, calculated for a proton beam at the energy step 70 with analogous experimental setup. The structure of the experimental degraded SOBP is correctly reproduced by the convoluted nominal SOBP using σ calculated at one specific energy, supporting the calculation (4.5). Being the degraded depth-dose distribution the result of a Gaussian filter, the average dose deposition in the plateau region is not affected by the degradation. The detailed view in Figure 6.15a shows how the ripples of the SOBP in water are smoothed by the Gaussian filter resulting in a flat plateau, correctly reproducing the experimental data. The most severe effect of the degradation is the widening of the distal fall-off. Figure 6.15b shows how the convolution approach is capable to reproduce the experimental data about the SOBP distal fall-off.

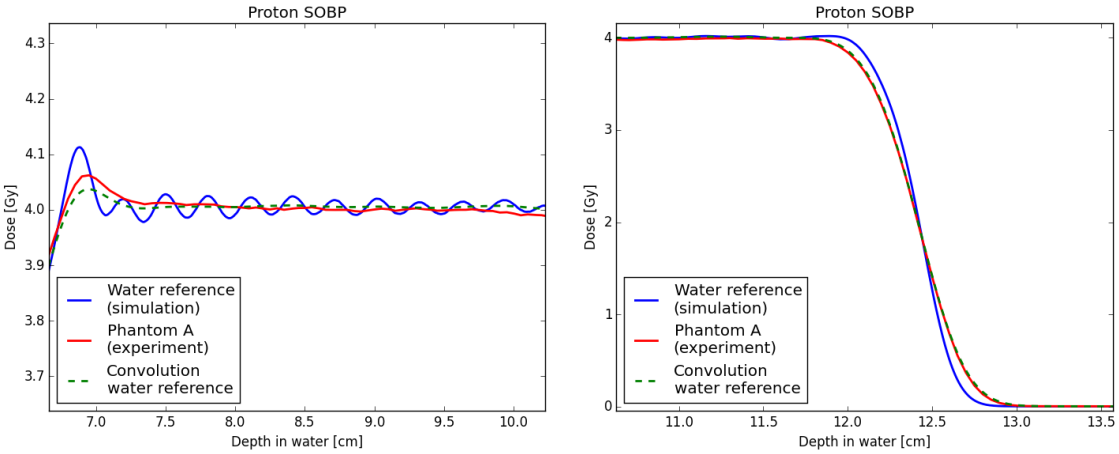

(a) (b)

Figure 6.15: Details of the SOBPs in Figure 6.14: (a) plateau region and (b) tail region.

6.4.2 Degradation effect on RBE

The scored LET spectra at different depths in water for the mixed fields including primaries and secondaries are plotted in Figure 6.18. The comparison of the water reference simulation to the transmission experiment on a lung-like phantom shows that the LET spectra present less pronounced peaks associated with a widening of the distributions. These effects are especially significant at the raising flank ($7.5cm$) and just upstream the peak position ($8.5cm$). Smaller, yet not negligible, differences in the spectra are observed at depths further from the peak. The low LET components of the reference and degraded spectra do no present any significant deviation. The resulting RBE and biological dose are reported in Table 6.7. For depths smaller than the peak position it is observed an increase of the RBE together with a decrease of the physical dose, compensating the biological effect. As a result, the relative deviations $D_{bio}^{\text{deg}}/D_{bio}^{(0)}$ are limited below $< 5\%$. The biggest effect is observed at the fall-off ($9.5cm$). Even if the LET spectra do not present major deviations, the simultaneous increase of the physical dose and of the RBE lead to an increase about $+16\%$ of the biological dose in this region. Finally, no significant deviations are observed at the tail of the Bragg peak. The deviations in the biological dose have to be compared with the ones in the physical dose $D^{\text{deg}}/D^{(0)}$, not including the RBE calculation. Here, the variations are not compensated or amplified by the RBE factor. Comparing the last two rows in Table 6.7 one observes that the trend of the positive or negative deviations in D_{bio}^{deg} is mainly determined by the trend of D^{deg}. The contribution of the RBE deviations, therefore, has a minor impact compared to the contribution of the physical dose deviations.

The dominant effect of the physical dose deviations on the biological effectiveness deviations observed when considering the RBE is confirmed by the behaviors of $fLET$ and $Q(LET)$ with respect to depth. These two tissue-independent physical quantities

Table 6.7: Results computation of RBE and biological dose for the reference and the degraded spectra at the considered depths. The last two rows of the table report the relative physical and biological dose between the nominal and degraded Bragg peak.

	$5\,cm$	$7.5\,cm$	$8.5\,cm$	$9.5\,cm$	$14.5\,cm$
$D^{(0)}[Gy]$	0.845	1.22	2.32	0.147	0.0549
$D^{\mathrm{deg}}[Gy]$	0.836	1.19	2.14	0.168	0.0538
$RBE^{(0)}$	$3.012 \pm .004$	$2.973 \pm .004$	$2.694 \pm .005$	$5.54 \pm .02$	$5.62 \pm .06$
RBE^{deg}	$3.024 \pm .004$	$3.001 \pm .004$	$2.775 \pm .008$	$5.56 \pm .02$	$5.63 \pm .07$
$D^{(0)}_{bio}[Gy]$	$2.532 \pm .006$	$3.64 \pm .01$	$6.27 \pm .02$	$0.81 \pm .01$	$0.31 \pm .01$
$D^{\mathrm{deg}}_{bio}[Gy]$	$2.535 \pm .006$	$3.61 \pm .01$	$5.99 \pm .01$	$0.94 \pm .01$	$0.31 \pm .01$
$D^{\mathrm{deg}}/D^{(0)}[\%]$	98.9	97.5	92.2	114.3	98.0
$D^{\mathrm{deg}}_{bio}/D^{(0)}_{bio}[\%]$	100.1	99.2	95.5	116.0	100.0

are indirectly available in FLUKA by scoring respectively the fluence with a LET scaling factor thorough the fluscw.f routine and the so-called DoseqLET. In the post-processing, the data is then respectively divided by the total fluence and by the physical dose in order to obtain the $fLET$ and $Q(LET)$ distributions with respect to depth. Moreover, $fLET$ and $Q(LET)$ do not represent directly the biological effect as for the RBE, but should rather be interpreted as a proxy for the biological effectiveness. The resulting distributions are reported in Figure 6.16 for the mono-energetic carbon beam and in Figure 6.17 for the carbon SOBP optimized from $3.5cm$ to $7.5cm$ on the physical dose in water. The plots show the comparison between the physical dose deposition, the fluence weighted LET and the radiation quality factor. For the mono-energetic beam, the behaviors of $fLET$ and $Q(LET)$ reproduce the trend of $RBE^{(0)}$ and RBE^{deg} observed in Table 6.7: a slight increase of $fLET$ and $Q(LET)$ in the degraded peak with respect to the reference case it is observed in the raising flank, a decrease at the peak position (not evaluated in Table 6.7), an increase about the distal falloff and finally compatible values in the low dose tail. The different scaling of the absolute and relative values have to be interpreted as the adoption of different models and algorithms to evaluate the biological effectiveness; nonetheless, the trend in over-estimating and under-estimating the effect results in an agreement between the RBE, $fLET$ and $Q(LET)$ approaches. The decrease of the effectiveness exactly at the pristine peak position ($z = 8.69cm$) has not a direct clinical relevance, since the mono-energetic carbon beam simulated should be replaced by a source having a wider energy distribution coupled with the presence of the ripple filter. Nonetheless, the reason for such decrease can be further investigated. To do so, an additional comparison of the LET spectra is performed at the pristine peak position ($z = 8.69cm$) and reported in Figure 6.19. The plot is separated from Figure 6.18 to allow for a more accurate interpretation of the values due to the different LET scale. Here, it is observed that the more abundant high LET interactions observed for the degraded distribution just upstream the peak ($z = 8.5cm$) result dominated by the high LET component of the undegraded peak, which energy deposition is concentrated

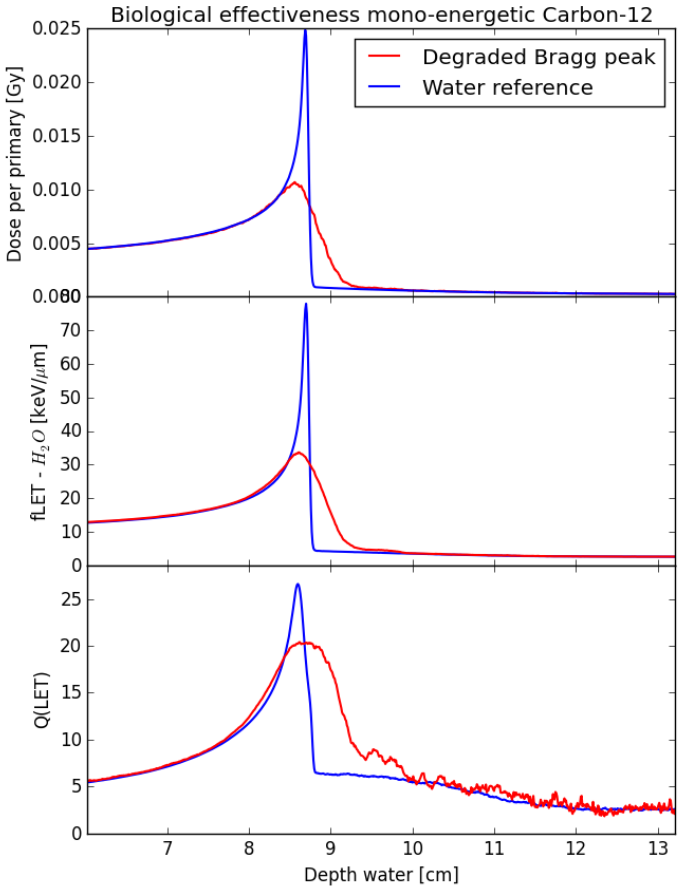

Figure 6.16: Comparison between the physical dose deposition, fluence weighted LET and radiation quality factor Q for a mono-energetic carbon beam. The undegraded distributions (blue) are reported together with the distributions downstream the lung like phantom defined by (5.3) (red). A common depth scale is adopted for the plots.

at this specific depth. As a result, the degraded peak presents a reduced biological effectiveness at the pristine peak position and at the same time a wider region of high biological effectiveness due to the presence of high LET interactions not only at the peak position but also about this specific depth. Again, in analogy to the Gaussian convolution of the physical dose, the biological effectiveness of a degraded Bragg peak results spread on a wider depth range and less peaked. As a matter of fact, no major deviations in the $fLET$ and $Q(LET)$ are observed between the undegraded and degraded SOBP in the plateau region in Figure 6.17. As for the physical dose, the most relevant deviations result about the distal falloff, mainly with an increased effectiveness about the tail.

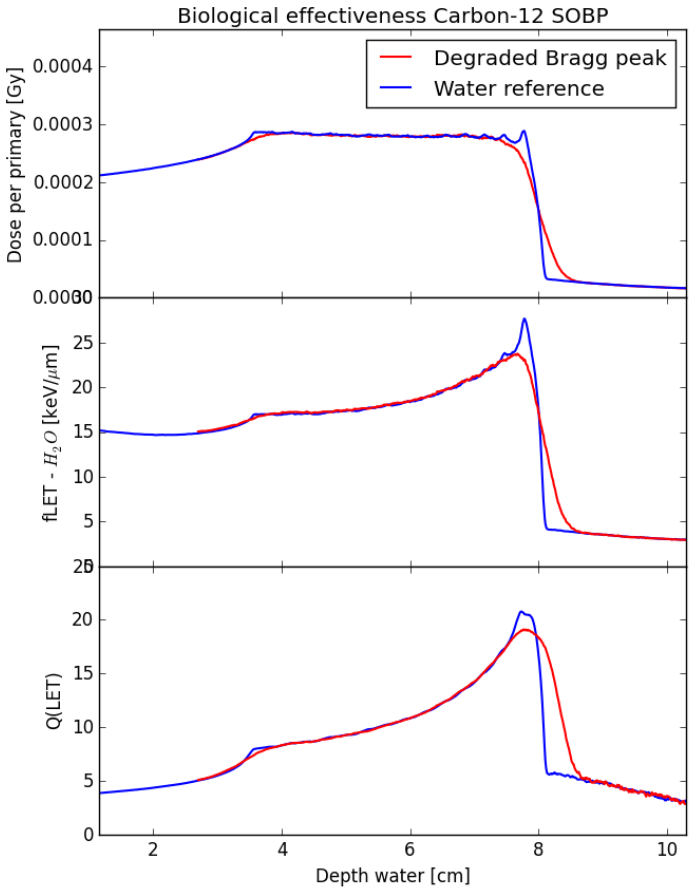

Figure 6.17: Comparison between the physical dose deposition, fluence weighted LET and radiation quality factor Q for a carbon SOBP optimized on the physical dose. The undegraded distributions (blue) are reported together with the distributions downstream the lung like phantom defined by (5.3) (red). A common depth scale is adopted for the plots.

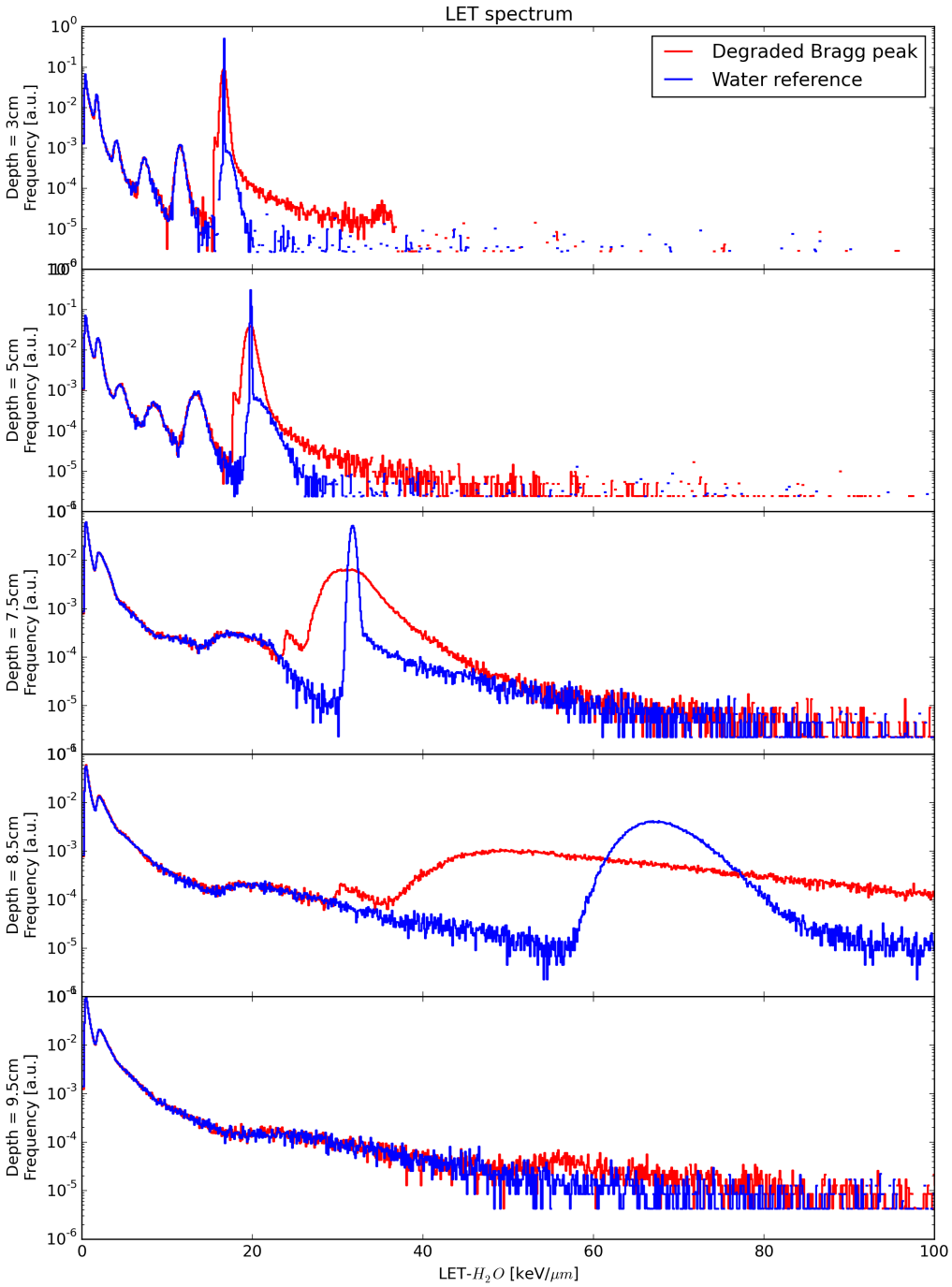

Figure 6.18: LET spectra in water at different positions of a ^{12}C Bragg peak. Comparison between the water reference (blue) and the result downstream a lung-like phantom generated with parameters (5.3) (red). The frequencies are reported with a logarithmic scale.

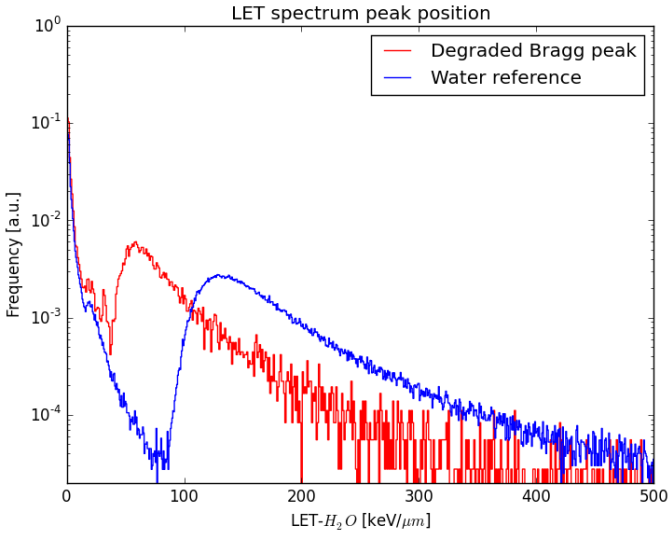

Figure 6.19: LET spectra in water at the pristine ^{12}C Bragg peak maximum ($z = 8.69cm$). Comparison between the water reference (blue) and the result downstream a lung-like phantom generated with parameters (5.3) (red). The frequencies are reported with a logarithmic scale.

Chapter 7

Conclusions and Outlook

In the following chapter the conclusions obtained from the discussed results and an outlook towards future work are presented.

Sources of degradation The Bragg peak degradation downstream stationary lung tissue is the result of several cumulative physic effects leading to a widening of the depth-dose distribution. So far, no detailed knowledge on the specific contribution of each phenomenon has been investigated with a solid study. Such information is fundamental in order to correctly characterize and predict the degradation. The separation of the effects presented in Figure 6.1 provides a clear assessment of the specific contributions. Previous degradation studies limited the analysis up to MCS and NS, i.e. check-board phantoms. The presented results show that the scattering effects contribute to the Bragg peak widening but are not the dominant effect. The scale of the degradation results determined by the presence of the fluctuations of the longitudinal water equivalent thickness within the transverse beam size.

Phantoms In order to optimize a systematic study of the degradation and also according to previous studies, the WET fluctuations have been differentiated in simple fluctuation ($\sigma^{2D}(WET)$) and complex fluctuation ($\sigma^{3D}(WET)$). The latter provides the most complete and accurate scenario. Nonetheless, the simple fluctuation results capable to reproduce all the relevant aspects of a degraded Bragg peak with a limited underestimation of the parameters. Given the reduced simulation time for $\sigma^{2D}(WET)$ phantoms, these result to be the most suitable setup for a systematic degradation study reproducing stationary lung parenchemya. Moreover, it results that a degradation study limited to regular check-board phantoms leads to a severe underestimation of the effect. The details reported in Appendix A show how a different behavior is obtained considering regular or randomized check-boards and, again, Figure 6.1 shows how even the randomized phantoms fail to correctly reproduce degraded Bragg peaks. Further limitations are due to the high sensitivity on the alignment in transmission experiments. Therefore, the applicability of such phantoms should be considered for the specific case of MC studies of the scattering effects, excluding an applicability for transmission experiments or for a systematic study of the total degradation.

Parametrization of degradation The description of the Bragg peak degradation by the width of the distal falloff and the peak-to-plateau ratio have the advantage of providing a direct interpretation of the results and to assess the effect of underdosage at the peak position or over-dosage in the tail region. However, given the z_{8020} and r_{peak} it is not possible to directly reproduce the whole shape of the degraded Bragg peak. Such aspect is relevant when aiming not only to the analysis of the effect but also to its prediction, which is the final objective of the project. Previous investigations suggested the use of a Gaussian filter on a nominal Bragg peak in order to obtain the degraded depth-dose distribution [3]. This approach is shown to be capable to correctly reproduce all the aspect observed in a transmission experiment through a lung-like phantom, as plotted in Figure 6.2. The use of a Gaussian convolution leads to several advantages: the degradation is described just with the parameter σ, on the other hand μ can be interpreted as the WET of the phantom, given the nominal Bragg peak at a specific energy[1] one can directly calculate the complete degraded depth-dose distribution analytically, the focus of the description is on the phantom avoiding biased conclusions due to the natural widening of the distribution at different energies for different particles, the method is robust considering the convolution over the whole depth-range and not on few points about the falloff or at the maximum. For these reasons and due to the capability of correctly reproducing the degradation, the description with the Gaussian filter should be preferred.

Gaussian filter description The results of the separation of the physical sources can be further interpreted. Considering the widening of the distal falloff, the effect of WET fluctuations appear to be more severe for ^{12}C beams compared to ^{1}p beams. This variation does not depend on the different interactions between the phantom and the beam particles, resulting in an unified description for the two beams. Applying the same Gaussian filter to the nominal proton and carbon depth-dose distributions having the same range, the widening of z_{8020} results more pronounced for the heavier particles. This is due to the fact that the undegraded falloff is sharper and the peak-to-plateau dose is bigger and, therefore, the application of a filter results in a severe smoothing of the distribution. On the other hand, the proton Bragg-peak is smoother and in a first approximation[2] can be considered as a Gaussian-filtered carbon peak, therefore the application of a second Gaussian filter results in a less severe smoothing. The description of the degradation with a Gaussian convolution directly leads to the conclusion that the most affected regions of the Bragg peak are the falloff and the maximum, due to the fact that these are surrounded by zones with a remarkable difference in the dose deposition. On the other hand, the raising flank and the low dose tail are almost not affected by the application of the filter. Moreover, the Gaussian description returns the parameter σ to describe the degradation, which is independent from the characteristics of the undegraded depth-dose distribution, allowing for a robust characterization independent from the intrinsic energy

[1]The nominal depth-dose distributions in homogeneous water are normally available in analytic TPS, being these the basic data-set to calculate the plans

[2]The approximation has to be considered only in order to interpret the effect of the Gaussian filter, without any specific physical meaning

straggling of the beam. In agreement with the fact that the scale of the degradation is mainly determined by $\sigma(WET)$ and not by nuclear or scattering interaction particle-dependent, it results that for a given phantom, σ is independent from the particle type and energy. The independence from the beam particle is observed experimentally in Table 6.3 and the independence from the energy is assesses via MC simulations and reported in Figure 6.10.

SOBP The independence from E_0 leads to a clinically relevant aspect: the description of the degradation of a SOBP. As developed in (4.5), $\partial\sigma/\partial E_0 = 0$ implies that the degraded SOBP is described directly by the convolution of the undegraded SOBP with a unique Gaussian filter. This is validated experimentally and reported in Figure 6.13. As a matter of fact, the most affected zone of a degraded SOBP is the distal falloff: this is, in first approximation, the result of the application of a Gaussian filter to a Heaviside step function. Therefore, a severe widening of the falloff is expected. On the other hand, no major effect is observed in the plateau region, resulting in a filtering of a constant function.

Range z_{80} The assessment of the particle range is fundamental for the development of novel techniques aiming to reduce the range uncertainties. Previous analytic calculations on proton beam show that the position on the falloff corresponding to 80% of the peak dose is a good estimator of the average particle range [13]. However, no explicit information in available for degraded Bragg peaks. Through MC techniques it is possible to have direct access to the range of the beam particles and project it on the corresponding position on the distal falloff. The results downstream an inhomogeneous lung-like phantom are reported in Table 6.2. This shows how, also for degraded depth-dose distributions, the value z_{80} is a good estimator of the particle range and can be adopted with a limited error. This is relevant in an experimental setup where one aims to predict or assess the particle range and has no direct access to the fluence with respect to depth.

Lung model and benchmark In order to perform a systematic study of the degradation downstream stationary lung parenchyma, a Monte Carlo analysis results the most suitable method. However, an experimental validation has to be performed in order to assess the capability of the code and of the $\sigma^{2D}(WET)$ phantoms to reproduce the experimental Bragg peak degradation. The benchmark requires three subsequent steps: the tuning of the MC beam parameters in order to reproduce the experimental ones, the selection of lung-like phantoms and the implementation of the phantoms in the MC simulations. For the first step, as reported in section 6.2.2, it is introduced a Gaussian spread in the momentum for the proton beam. This approach fails for carbon beams, resulting in an underestimation of the raising flank. This should be interpreted as the missing description of a mixed particle field including lighter particles resulting from the interaction of the primary ^{12}C with the BAMS. This leads to a more complex source that is properly described by a complete phase space, which is necessary to adopt for a carbon beam. Nonetheless, a slight

underestimation in the raising flank is observed also with the adoption of the PS and has to be attributed to the precision in the implementation of the nuclear interaction models in the FLUKA code. The selection of the benchmark lung-like phantom has to satisfy multiple requirements: reproducibility of the experiment, flexibility in the setup, advanced knowledge of the internal structure and affinity to a real lung. The adoption of an animal lung sample guarantee a real lung degradation but compromises the other requirements, which are on the other hand respected by 3D printed phantoms to the detriment of a real lung degradation. A good compromise is obtained adopting porous materials. A detailed analysis shows that the internal structure of the Gammex lung phantom is comparable to the one of a aerated concrete of similar density, leading to a wider spectrum of phantoms available for the MC benchmark. To investigate the microscopic properties of the porous phantoms the most reliable method resulted to be a high resolution μCT scan, allowing to resolve the internal structures and determine the air to solid volume fraction. The most reliable method to evaluate the density results to be a study on the water equivalent thickness of the phantom simulated in a transmission experiment. The use of the μCT, the caliper to get the macroscopic dimension and WET for the density provides independent methods to measure the physical properties of the phantom, allowing for a robust implementation in the MC code. Finally, the implementation of the phantoms in FLUKA according to the $\sigma^{2D}(WET)$ model results capable to reproduce the experimental degradation of an analogous transmission experiment. The use of the phantoms reproducing simple fluctuations of the water equivalent thickness produces, as expected, an underestimation of the the degradation with respect to the experimental data. However, the underestimation is reduced to few percent points when considering parameters such as the distal falloff z_{8020} and, moreover, the overall shape of the degraded Bragg-peak is correctly reproduced. This phantom geometry is capable not only to reproduce one specific phantom degradation, but also to take in account for the different effect given by a varying air filling, dimension of internal structures and elemental composition. These properties are combined with a compact but at the same time complete definition of the internal geometry and with a high flexibility in the design of the phantom with respect to macroscopic and microscopic characteristics. Therefore, the $\sigma^{2D}(WET)$ model implemented in FLUKA satisfies the requirements to be adopted for the systematic study of the degradation.

Description of degradation The implementation of the degradation effect in an analytic TPS requires an advanced knowledge on the variations to be applied to the nominal depth-dose distributions for each specific treatment. The Gaussian convolution model provides a simple and compact but yet complete tool to obtain the final depth-dose distribution. The dependencies of σ on specific lung and beam parameters are reported in Table 6.6. The simulation data obtained with the $\sigma^{2D}(WET)$ phantoms is interpolated with a minimum use of free parameters, according to the expected dependencies and to the constraints given by the limits $x_i \to 0$. It results an excellent agreement with a square root dependency on the water equivalent thickness of the traversed lung tissue, as proposed in previous works. The dependencies on the

other parameters have not being investigated so far and good agreement is obtained with the functions adopted. The special case of the simultaneous variation of the WET and the air filling of the lung parenchyma suggests that multiple variations are described by a factorization of the single dependencies, rather than a linear combination. The precise knowledge of the single and coupled dependencies allow to tune the degradation to specific lung cases. The approach is proved to be successful trying to retrospectively infer the σ of the phantom used to assess the physical sources of degradation, even beyond the investigated range of the parameters.

Degradation RBE A complete implementation in a clinical setting requires to assess the effect of the modification of the energy and LET spectra due to the degradation on the RBE and therefore on the biological dose. The analysis on a reference lung case shows that the observed deviations in the LET spectrum result in a slight but yet not negligible change in the RBE compared to the nominal case. However, the trend of under-dosage or over-dosage for the biological dose at specific depths is mainly determined by the deviations in the physical dose deposition with a small contribution of the deviations in RBE. Compatible results are obtained when considering the $fLET$ and $Q(LET)$ as tissue independent estimators of the biological effectiveness, both for a mono-energetic and for a carbon SOBP. For the latter, the most significant deviations are observed about the distal falloff.

TPS implementation The future application of the results relies on an implementation of the knowledge on the degradation in an analytic planning system. The discussed material refers to the sole stationary lung parenchyma, which occupies the greatest volume of the human lung but has to be coupled with other macroscopic structures and respiratory motion. The results on the physical sources of the degradation showed how deviations in the WET provide the most severe effect, therefore macroscopic structures (e.g. veins) resolvable with a clinical CT have to be considered simultaneously by the TPS. The dependencies on lung parenchyma parameters should then be used to calculate the corresponding σ knowing the track of the particles and providing the information concerning the presence of an inhomogeneous or homogeneous tissue. Moreover, the degradation can be tuned on specific lung parameters such as the air filling or the total density. Future transmission experiments on animal lungs could then be interpreted joining the capability of the TPS to take in account macroscopic structures and the implementation of degradation for pathways through lung parenchyma not resolvable with a clinical CT. A complete description of a lung treatment should finally include a modeling of the respiratory motion, taking in account as well the different degradation resulting from a different air filling phase of the parenchyma. The implementation of the effect will result, as suggested by the convolution description, in small deviations in the plateau of the SOBP and mainly in over-dosage beyond the distal falloff, which correct implementation in a clinical TPS will improve the sparing of organs at risk distal to the target volume.

Appendix A

Suitability of check-board phantoms

In this appendix, the applicability of check-board phantoms for degradation studies is assessed.

Previous studies investigated the Bragg peak degradation due to regular check-board phantoms with MC simulations [2] and with transmission experiments [37]. This phantom geometry allows for well defined structures, which regularity can be exploited to infer the resulting effect. As a matter of fact, Sawakuchi et. al. concluded that the corresponding degradation is mainly generated by MCS with just a small ($\sim 5\%$) contribution of NS. Such conclusion is possible since, in a regular check-board

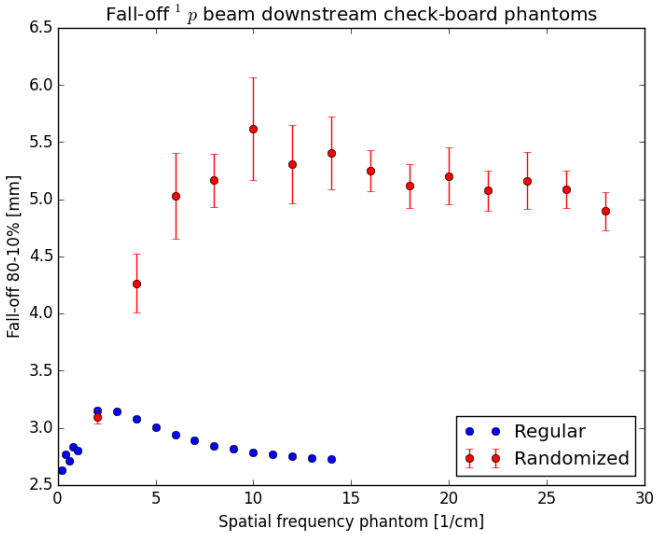

Figure A.1: Comparison distal fall-off for ^1p beam downstream check-board phantoms generated according to [2]. The blue points correspond to regular phantoms and the red ones to randomized phantoms.

phantom, there is no fluctuation of the thickness in the z-direction depending on the entrance point; therefore, the range straggling and the scattering effects have to be

considered the sole sources of degradation. Aiming for a more complex geometry towards the lung case, it is performed an extension of a previous study [2]. The simulation setup analogous, i.e. a monoenergetic ^1p beam is simulated through check-board phantoms filled 50% with air and 50% with compact bone having a total z-dimension of $10cm$. The step-size range is extended and it is reduced down to $d = 0.06cm$ for regular phantoms and to $d = 0.03cm$ for randomized phantoms. The randomization process respect the constraint of having a fixed number of solid and air elements in the z-direction at each entrance point, avoiding the fluctuations in thickness. The resulting fall-off degradation is reported in Figure A.1 with respect to the spatial frequency of the phantoms ($f = 1/d$). The regular-phantom degradation is the result of a single MC simulation for each data point; whereas, the randomized-phantom degradation data is the result of multiple ($n > 10$) randomizations of the phantoms and corresponding MC simulation for each data point, in order to calculate the average value of the fall-off and its standard deviation.

The data reported in Figure A.1 shows how the adoption of regular check-boards results in an underestimation of the degradation compared to the randomized case. The trend of the fall-off width shows an increase until a maximum value followed by a decrease at high spatial frequencies, suggesting that in the limit $d \to 0$ or $f \to +\infty$ the check-board phantom appears as a homogeneous mixture of the basic components resulting in the sole range straggling degradation. The maximum value is observed at higher spatial frequencies for the randomized structures. The data presented in Figure A.1 and in Figure 6.1a leads to the conclusion that check-board phantoms are not suitable for a systematic investigation of the degradation downstream lung tissue, due to the underestimation of the effect. Such phantoms, due to the well defined geometry, have to be considered within the frame of the separation of the physical sources of degradation as an intermediate step between the nominal Bragg peak and the final lung-tissue degradation.

Moreover, an experimental setup with this particular phantom geometry is extremely sensible to misalignment, leading to systematic errors in a transmission experiment. Previous experiments at HIT report the presence of a second smaller peak in the tail of the Bragg dose distribution downstream a check-board phantom. Such second peak reduces or vanishes repeating the experiment with a new alignment of the phantom [37]. A Monte Carlo study is performed in order to investigate the origin of the second peak, concluding that a slight misalignment can lead to systematic deviations of the WET in the z-direction depending on the (x, y) entrance point and therefore a second peak. This effect, together with the difficulties in producing the exact geometry reported in section 6.2.5, lead to the conclusion that check-board phantoms should be preferentially considered in MC simulations and avoided in experimental setups.

Bibliography

[1] M. Urie, M. Goitein, W. R. Holley, and G. T. Y. Chen, "Degradation of the bragg peak due to inhomogeneities," *Physics in Medicine and Biology*, vol. 31, no. 1, p. 1, 1986.

[2] G. O. Sawakuchi, U. Titt, D. Mirkovic, and R. Mohan, "Density heterogeneities and the influence of multiple coulomb and nuclear scatterings on the bragg peak distal edge of proton therapy beams," *Physics in Medicine and Biology*, vol. 53, no. 17, p. 4605, 2008.

[3] M. Witt, "Modulationseffekte von Kohlenstoff Ionen bei der Bestrahlung von Lungen", *Technischen Hochschule Mittelhessen*, 2014.

[4] L. Liang, E. W. Larsen, and I. J. Chetty, "An anatomically realistic lung model for monte carlo-based dose calculations," *Medical Physics*, vol. 34, no. 3, pp. 1013–1025, 2007.

[5] H. Johns and J. Cunningham, *The Physics of Radiology.* American Lecture Series, Publication No. 932. a Monograph in, Thomas, 1974.

[6] R. R. Wilson, "Radiological use of fast protons," *Radiology*, vol. 47, no. 5, pp. 487–491, 1946. PMID: 20274616.

[7] U. Amaldi and G. Kraft, "Radiotherapy with beams of carbon ions," *Reports on Progress in Physics*, vol. 68, no. 8, p. 1861, 2005.

[8] NIST database. Available from: www.nist.gov/pml/data/asd.cfm.

[9] E. Segrè, *Nuclei and particles: an introduction to nuclear and subnuclear physics.* W. A. Benjamin, 1977.

[10] K.A. Olive et al. (PDG), Chin. Phys. C38, 090001 (2014) (http://pdg.lbl.gov).

[11] J. F. Ziegler, "Stopping of energetic light ions in elemental matter," *Journal of Applied Physics*, vol. 85, no. 3, pp. 1249–1272, 1999.

[12] C. Möhler, P. Wohlfahrt, C. Richter, and S. Greilich, "Range prediction for tissue mixtures based on dual-energy CT," *Physics in Medicine and Biology*, vol. 61, no. 11, p. N268, 2016.

[13] T. Bortfeld, "An analytical approximation of the Bragg curve for therapeutic proton beams," *Medical Physics*, vol. 24, no. 12, pp. 2024–2033, 1997.

[14] R. Evans, *The Atomic Nucleus*. @Internat. S.in P. & A. Physics, McGraw-Hill, 1955.

[15] H. A. Bethe, "Molière's theory of multiple scattering," *Phys. Rev.*, vol. 89, pp. 1256–1266, Mar 1953.

[16] H. W. Lewis, "Multiple scattering in an infinite medium," *Phys. Rev.*, vol. 78, pp. 526–529, Jun 1950.

[17] A. Ferrari, P. Sala, R. Guaraldi, and F. Padoani, "An improved multiple scattering model for charged particle transport," *Nuclear Instruments and Methods in Physics Research Section B: Beam Interactions with Materials and Atoms*, vol. 71, no. 4, pp. 412 – 426, 1992.

[18] S. Sachs, Lecture BIO 205, Cuesta College-Human Anatomy. Available from: http://bit.ly/2aQ3D5N.

[19] E. R. Weibel and D. M. Gomez, "Architecture of the human lung," *Science*, vol. 137, no. 3530, pp. 577–585, 1962.

[20] U. Titt, M. Sell, J. Unkelbach, M. Bangert, D. Mirkovic, U. Oelfke, and R. Mohan, "Degradation of proton depth dose distributions attributable to microstructures in lung-equivalent material," *Medical Physics*, vol. 42, no. 11, pp. 6425–6432, 2015.

[21] M. O. et al., "The number of alveoli in the human lung," *American Journal of Respiratory and Critical Care Medicine*, vol. 169, no. 1, pp. 120–124, 2004.

[22] U. Schneider, B. Schaffner, T. Lomax, E. Pedroni, and A. Tourovsky, "A technique for calculating range spectra of charged particle beams distal to thick inhomogeneities," *Medical Physics*, vol. 25, no. 4, pp. 457–463, 1998.

[23] B. Schaffner, E. Pedroni, and A. Lomax, "Dose calculation models for proton treatment planning using a dynamic beam delivery system: an attempt to include density heterogeneity effects in the analytical dose calculation," *Physics in Medicine and Biology*, vol. 44, no. 1, p. 27, 1999.

[24] K. Parodi, A. Mairani, S. Brons, B. G. Hasch, F. Sommerer, J. Naumann, O. Jkel, T. Haberer, and J. Debus, "Monte carlo simulations to support start-up and treatment planning of scanned proton and carbon ion therapy at a synchrotron-based facility," *Physics in Medicine and Biology*, vol. 57, no. 12, p. 3759, 2012.

[25] A. Ferrari, P. R. Sala, A. Fasso, and J. Ranft, "FLUKA: A multi-particle transport code (Program version 2005)," 2005.

[26] T. T. Böhlen, F. Cerutti, M. P. W. Chin, A. Fassò, A. Ferrari, P. G. Ortega, A. Mairani, P. R. Sala, G. Smirnov, and V. Vlachoudis, "The FLUKA Code: Developments and Challenges for High Energy and Medical Applications," *Nuclear Data Sheets*, vol. 120, pp. 211–214, June 2014.

[27] R. M. Sternheimer, S. M. Seltzer, and M. J. Berger, "Density effect for the ionization loss of charged particles in various substances," *Phys. Rev. B*, vol. 26, pp. 6067–6076, Dec 1982.

[28] HIT website. Available from: https://www.klinikum.uni-heidelberg.de/.

[29] S. E. Combs, M. Ellerbrock, T. Haberer, D. Habermehl, A. Hoess, O. Jkel, A. Jensen, S. Klemm, M. Mnter, J. Naumann, A. Nikoghosyan, S. Oertel, K. Parodi, S. Rieken, and J. Debus, "Heidelberg ion therapy center (hit): Initial clinical experience in the first 80 patients," *Acta Oncologica*, vol. 49, no. 7, pp. 1132–1140, 2010.

[30] Gammex, Tissue Equivalent Materials Gammex 450, 452, 453, 454, 455, 456, 481, 482. Available from: http://bit.ly/2cst6mn.

[31] N. Huenemohr, B. Krauss, C. Tremmel, B. Ackermann, O. Jaekel, and S. Greilich, "Experimental verification of ion stopping power prediction from dual energy CT data in tissue surrogates," *Physics in Medicine and Biology*, vol. 59, no. 1, p. 83, 2014.

[32] S. H. Kim, B. K. Kim, and H. Lim, "Effect of isocyanate index on the properties of rigid polyurethane foams blown by hfc 365mfc," *Macromolecular Research*, vol. 16, no. 5, pp. 467–472, 2008.

[33] T. Tessonnier, T. Marcelos, A. Mairani, S. Brons, and K. Parodi, "Phase space generation for proton and carbon ion beams for external users applications at the Heidelberg ion therapy center," *Frontiers in Oncology*, vol. 5, p. 297, 2016.

[34] M. Kraemer and M. Scholz, "Treatment planning for heavy-ion radiotherapy: calculation and optimization of biologically effective dose," *Physics in Medicine and Biology*, vol. 45, no. 11, p. 3319, 2000.

[35] ICRP, 1991. 1990 Recommendations of the International Commission on Radiological Protection. ICRP Publication 60. Ann. ICRP 21 (1-3).

[36] A. Rotondi, P. Pedroni, and A. Pievatolo, *Probabilita, statistica e simulazione. 3rd edition.* Springer, 2011.

[37] L. Polster, "Measurement of inhomogeneiry effects in dual energy computed tomography used for ion beam therapy planning", *Project report - Mannheim University*, 2015.

Acknowledgments

In this last section of the thesis I would like to thank all the people and institutions that made this work possible.

Prof. Dr. Oliver Jäkel for giving me the possibility to work in his department at the German Cancer Research Center (DKFZ), which was a motivating environment to investigate a long term research project. Thanks to the support provided by the department it was possible to present part of this thesis work at the international conference PTCOG55 in Prague (Czech Republic) during May 2016.

Prof. Dr. Peter Bachert for being the supervisor of my thesis at the department of Physics and Astronomy at the Heidelberg University and for providing me important recommendations not only related to the thesis, but also towards my future career as physicist.

Dr. Steffen Greilich for giving me the possibility to work in his group and develop this project. I would especially like to thank him for the continuous support he provided me with an extreme dedication and carefulness, showing all the passion associated with his work.

Christian Möhler for the remarkable time invested in fundamental meetings and discussions even though my project, originally thought as directly connected to his investigations, turned out to be on an slightly independent branch.

The members of DKFZ and HIT who supported me at different stages of the project. Among others, I would like to thank Dr. Andrea Mairani for introducing me to the use of FLUKA, Dr. Mark Bangert for the useful discussions about future TPS implementation, Dr. Jugold Manfred for the acquisition and the interpretation of the μCT scans, Dr. Stephan Brons for the experimental sessions at HIT.

Dr. Ulrich Weber and Dr. Matthias Witt for the discussions based on their previous studies at GSI that lead to the adoption of the Gaussian filter description of the degradation.

The German Academic Exchange Service (DAAD) that supported me during the two years as a master student in Heidelberg and made this work possible. This was not just mere financial support, but it also provided me the chance to get directly involved in the German culture and meet many international students.

My colleagues at DKFZ for the time spent in meetings providing reciprocal support, seminars, conferences and as well for the pleasant time not only in science-related events.

My old friends in Italy who keep involving me as if I was there; even if, by now, I have been living abroad for more than two years. My new friends in Heidelberg that

made this time not only a scientific but also a personal growth.

My girlfriend Alice who has always been at my side supporting me in both quiet and difficult moments, in particular before the PTCOG conference and towards the end of the thesis.

My family to whom this thesis is dedicated. Even if my passion for this subject took me physically faraway from them, they never let me feel distant on a personal level. A special thanks goes to my father, who also advised me in the investigation for a porous lung-like material, leading to the adoption of the so-called Phantom C.

Erklärung:

Ich versichere, dass ich diese Arbeit selbstständig verfasst habe und keine anderen als die angegebenen Quellen und Hilfsmittel benutzt habe.

Heidelberg, den 21.10.2016 .....

Riccardo Dal Bello